

# A hard-sphere model on generalized Bethe lattices: Statics

Hendrik Hansen-Goos<sup>1</sup> and Martin Weigt<sup>2</sup>

<sup>1</sup>*Institut für Theoretische Physik, Universität Göttingen,  
Friedrich-Hund-Platz 1, D-37077 Göttingen, Germany*

<sup>2</sup>*Institute for Scientific Interchange, Viale Settimio Severo 65, I-10133 Torino, Italy*  
(Dated: October 26, 2018)

We analyze the phase diagram of a model of hard spheres of chemical radius one, which is defined over a generalized Bethe lattice containing short loops. We find a liquid, two different crystalline, a glassy and an unusual crystalline glassy phase. Special attention is also paid to the close-packing limit in the glassy phase. All analytical results are cross-checked by numerical Monte-Carlo simulations.

PACS numbers: 64.70.Pf, 64.60.Cn, 75.10.Nr

## I. INTRODUCTION

Even after many years of vivid interest, the structural glass transition is still an open and alive topic of research [1, 2, 3, 4, 5]. Being defined by a drastic slowing down of the equilibration time of a liquid, it is introduced as a dynamical, non-equilibrium phenomenon. Up to now it is, however, one of the crucial questions if this slowing down is accompanied by an equilibrium glass transition or not.

Recently, lattice-gas models have played an increasing role in this discussion [6, 7, 8, 9]. The central idea of these models is to incorporate *static geometrical constraints* via hard-sphere interactions which restrict the possible particle packings and introduce some kind of geometrical frustration. Defined on (generalized) Bethe lattices, these models are characterized by the existence of a dynamical glass transition, followed by a static one.

These models are contrasted by the so-called *kinetically constrained* models [4], in which not all particle moves are permitted, but which are characterized by a trivial thermodynamic equilibrium behavior. Defined on a Bethe lattice, they show, however, a very similar dynamical behavior to the above mentioned models [10].

The model analyzed in this paper was introduced in [7], and it belongs to the class of geometrically constrained models. Its equilibrium behavior will be analyzed in great detail using the cavity method [11, 12]. The model can be defined over any lattice or graph. Sites are either occupied by particles, or they are empty. The particles are, however, too large to allow any two neighboring sites to be occupied simultaneously. In the presence of short loops in the lattice, this hard-core exclusion is sufficient to create a very rich phase diagram, including a liquid, two different crystalline, a glassy and an unusual, crystalline glassy phase. Whereas this paper concentrates completely on the static properties of the model, a subsequent publication [13] will consider the dynamics.

The paper is organized as follows: In the next section, the model is defined. Sec. III is dedicated to a description of an iterative method for the calculation of the partition function, or more precisely of effective local fields. Sec. IV solves this iterative method for the liquid-crystal transition, whereas Secs. V and VI are dedicated to the glass phase. Conclusion and outlook are given in the last section.

## II. THE MODEL

The model was already introduced and studied in [7]. In its most general formulation, it is defined on a graph  $G$  having vertices  $V = \{1, \dots, N\}$  and undirected edges  $\{i, j\} \in E$  connecting pairs of vertices. Vertices can either be empty,  $n_i = 0$ , or they are occupied by a particle,  $n_i = 1$ . These particles interact via a hard core of chemical radius one, i.e. neighboring vertices cannot be occupied simultaneously by two particles. Formulated in a more formal way, all edges  $\{i, j\} \in E$  fulfill the constraint  $n_i n_j = 0$ , i.e. one of the end vertices has to be empty. The model can thus be characterized by its grand-canonical partition function

$$\Xi(\mu) = \sum_{n_1, \dots, n_N \in \{0, 1\}} e^{\mu \sum_{i=1}^N n_i} \prod_{\{i, j\} \in E} (1 - n_i n_j), \quad (1)$$

or its grand-canonical potential

$$\Omega = -\frac{1}{\mu} \ln \Xi. \quad (2)$$

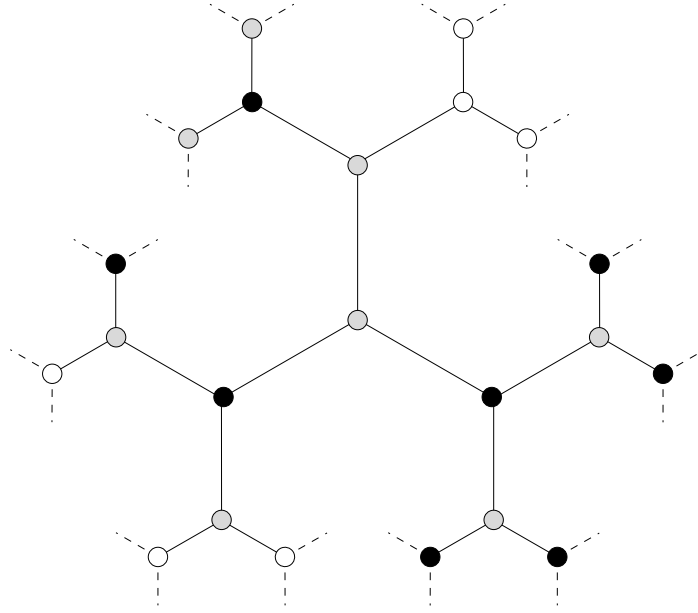


FIG. 1: Part of a Bethe lattice with  $k = 2$ . Black vertices mark occupied sites, gray ones cannot be occupied due to volume exclusion. The lower right branch shows the densest local packing.

Here we have introduced the chemical potential  $\mu$  which is coupled to the total particle number  $\sum_i n_i$  and can thus be used to regulate the particle density

$$\rho = \frac{1}{N} \sum_{i=1}^N n_i. \quad (3)$$

Note that the product over all edges in Eq. (1) serves as an indicator function for allowed particle configurations: Whenever there is at least one pair of occupied adjacent vertices, the product vanishes and thus the configuration does not contribute to the partition function. Note also that due to the hard-core interaction between particles the temperature does not play any role in the model, without loss of generality it is set to one.

So far, the model is still defined on a general graph. In this work we will concentrate on (generalized) Bethe lattices. Bethe lattices can be defined in two different ways:

- The first definition considers a Bethe lattice as an infinite regular tree, i.e. a cycle-free graph of fixed vertex degree (or coordination number)  $k + 1$ . The hard-sphere model on this graph was first considered by Runnels [14].
- As a second possibility we can define a Bethe lattice as a random  $(k + 1)$ -regular graph of  $N$  vertices, with  $N \rightarrow \infty$  in the thermodynamic limit. This version is frequently used in the context of glassy systems [12], and allows in particular for the simulation of finite systems.

Locally, both systems are equivalent due to the fixed vertex degree, the case  $k = 2$  together with a possible particle packing is visualized in Fig. 1. The crucial difference results from the existence of cycles in random graphs: Even if these are of length  $\mathcal{O}(\ln N)$ , i.e. their length diverges for large  $N$ , they are in general inconsistent with the crystalline structure which will be considered in Sec. IV. A densest particle packing on a Bethe lattice defined as an infinite tree consists of an alternation of occupied and empty sites. In random regular graphs, many cycles of odd length exist, preventing this alternating configuration from being globally feasible. A way out of this dilemma will be discussed later on.

Realistic, i.e. finite-dimensional, systems contain, however, many short cycles. To imitate this, we generalize Bethe lattices in the following way, cf. also Fig. 2: The graph is composed of cliques, i.e. fully connected subgraphs of  $p + 1$  vertices each. In each vertex,  $k + 1$  of these cliques merge, such that the resulting graph has constant vertex degree  $p(k + 1)$ . The global structure resembles, however, a Bethe lattice: We assume that besides the loops inside the cliques there are no other short cycles. Note that ordinary Bethe lattices are obtained in the special case  $p = 1$ , which is included in the following discussion of the general case. Also generalized Bethe lattices can be defined in the two ways discussed above, with similar consequences on the global feasibility of locally dense packings.

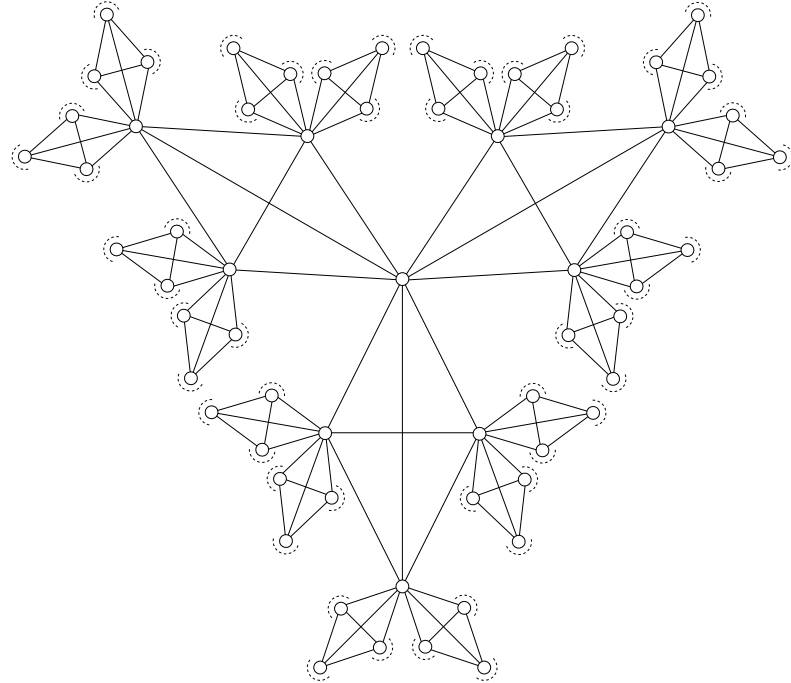


FIG. 2: Part of a generalized Bethe-lattice with  $k = 2$ ,  $p = 3$ . The 21 cliques connecting the central vertex to its nearest and second neighbors are shown.

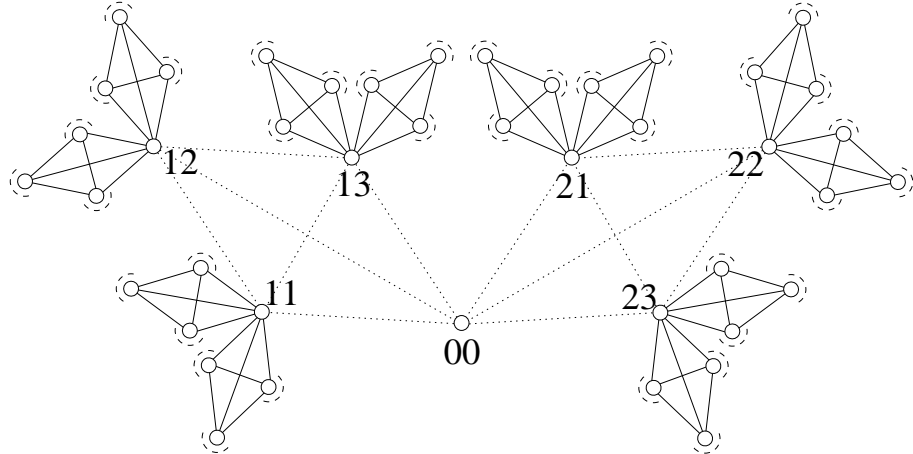


FIG. 3: Iteration of rooted trees:  $k = 2$  branches of  $p = 3$  rooted trees are merged to form a new tree with root 00.

### III. ITERATION OF THE PARTITION FUNCTION

The direct calculation of the partition function is complicated. It can, however, be achieved via an iterative method. For doing so, we shall introduce the notation of a *rooted subtree*: Imagine one of the cliques containing a vertex  $i$  to be removed from the graph, then a rooted subtree consists of the connected component containing  $i$ . The vertex  $i$  itself is denoted as the root of the subtree, cf. Fig. 3. Note that the root has only  $kp$  neighbors, whereas all other vertices in the subtree have degree  $(k+1)p$ . For each of these rooted trees we introduce two restricted partition functions:  $\Xi_e^i$  denotes the partition function with  $n_i$  fixed to zero, whereas  $\Xi_*^i$  corresponds to an occupied root.

Given  $kp$  rooted trees ( $j = 1, \dots, k$ ,  $l = 1, \dots, p$ ), these can be composed according to Fig. 3 to form one new rooted tree with root  $j = 0$ ,  $l = 0$ . The double index is introduced to lighten the notation in the following equations: The first index defines the (removed) clique containing the root, whereas  $k$  enumerates the vertices within this clique. The

restricted partition function of the new tree can now be easily inferred from those of the  $kp$  original ones:

$$\Xi_e^{00} = \prod_{j=1}^k \left( \prod_{l=1}^p \Xi_e^{jl} + \sum_{l=1}^p \Xi_*^{jl} \prod_{\substack{m=1 \\ m \neq l}}^p \Xi_e^{jm} \right) \quad (4i)$$

$$\Xi_*^{00} = e^\mu \prod_{j=1}^k \left( \prod_{l=1}^p \Xi_e^{jl} \right). \quad (4ii)$$

The expression in the brackets stands for the contribution of one branch: In case that the root 00 is empty, up to one of the neighbors in each branch can be occupied. If, on the other hand, the root is occupied, none of its neighbors is allowed to be occupied. The additional factor  $e^\mu$  in the second equation takes into account the chemical potential acting on the root particle.

Introducing now the *cavity fields*

$$x^{jl} \doteq \frac{\Xi_*^{jl}}{\Xi_e^{jl}} \quad (5)$$

(more precisely,  $\ln(x^{jl} + 1)/\mu$  defines a local field coupled to  $n_{jl}$ ), we find

$$\begin{aligned} x^{00} &= \frac{e^\mu}{\prod_{j=1}^k (1 + \sum_{l=1}^p x^{jl})} \\ &\doteq \hat{x}(x^{11}, x^{12}, \dots, x^{kp}). \end{aligned} \quad (6)$$

In order to understand the thermodynamic behavior of our model, we have to find appropriate solutions to these equations. In the next section, we shall discuss the case of the transition toward an ordered, crystalline phase, whereas Sec. V is dedicated to glassy solutions.

Before doing so, we have to clarify the physical meaning of  $x^{jl}$  and its connection to observables of the system. A simple observable is given by the local density  $\rho^{00}$  of vertex 00. This quantity can be obtained by composing rooted subtrees as well. In the original graph, each vertex has, however,  $(k+1)p$  neighbors. Within one iteration step, this can be achieved by merging  $(k+1)$  instead of  $k$  branches. Denoting the corresponding partition functions by  $\tilde{\Xi}_{e/*}^{00}$ , we get

$$\tilde{\Xi}_e^{00} = \prod_{j=1}^{k+1} \left( \prod_{l=1}^p \Xi_e^{jl} + \sum_{l=1}^p \Xi_*^{jl} \prod_{\substack{m=1 \\ m \neq l}}^p \Xi_e^{jm} \right) \quad (7i)$$

$$\tilde{\Xi}_*^{00} = e^\mu \prod_{j=1}^{k+1} \left( \prod_{l=1}^p \Xi_e^{jl} \right). \quad (7ii)$$

This results in

$$\frac{\rho^{00}}{1 - \rho^{00}} = \frac{\tilde{\Xi}_*^{00}}{\tilde{\Xi}_e^{00}} = \frac{e^\mu}{\prod_{j=1}^{k+1} (1 + \sum_{l=1}^p x^{jl})}, \quad (8)$$

i.e. physical observables can be directly calculated from the cavity fields.

## IV. CRYSTALLIZATION

### A. Liquid and crystalline solutions

To solve Eq. (6), we have to restrict the solution space by considering the limiting cases  $\mu \rightarrow \pm\infty$ . For the moment we discuss only the first case for the definition of the generalized Bethe lattice, i.e. we exclude the existence of long loops which may have some influence on the global packing structure.

The limiting case of an empty (or very dilute) system ( $\mu \rightarrow -\infty$ ) is characterized by a spatially homogeneous density describing a *liquid* phase. Consequently, the cavity fields are all equal to some  $x^*$  given self-consistently by  $x^* = \hat{x}(x^*, \dots, x^*)$ .

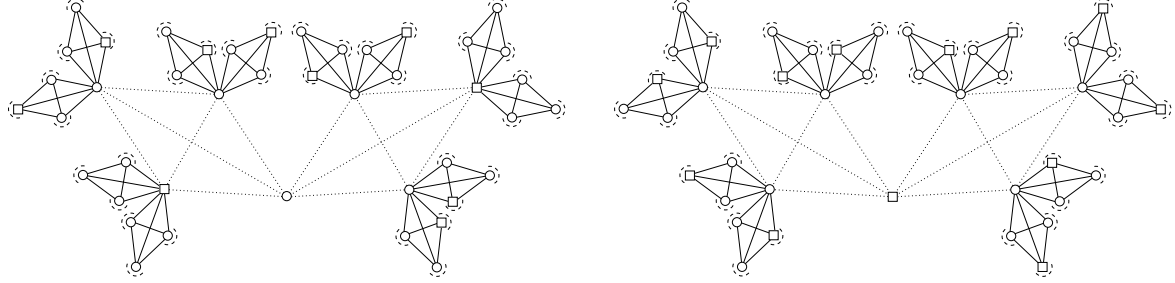


FIG. 4: Possible iteration steps leading to rooted trees with root in the 0-lattice (left), 1-lattice (right). Vertices belonging to the 0-lattice (1-lattice) are depicted by  $\circ$  ( $\square$ ).

In the limit  $\mu \rightarrow \infty$  we have to search for close-packings of the system. In these every clique carries exactly one particle, due to their regular structure these configurations are to be considered as being *crystalline*. The number of these configurations is exponential in the size of the graph (*i.e.* the number of sites), as can be seen easily: Initializing the configuration by putting one particle on an arbitrary vertex, all neighboring vertices have to be free. The  $(k+1)kp^2$  second neighbors are partitioned into  $(k+1)kp$  cliques of  $p$  vertices each, and each of these cliques can carry exactly one particle - so there are  $p^{(k+1)kp}$  possible configurations for selecting the particle positions in between the second neighbors. Iterating this argument, we obviously find an exponential number of close-packings.

Selecting one close-packing, we can identify two sub-lattices: The first is formed by the occupied vertices (1-lattice), the second by the empty vertices (0-lattice). We introduce two cavity fields  $x^{(0)}$  and  $x^{(1)}$  for the sub-lattices. Note that a more general ansatz that works with  $p+1$  different cavity fields corresponding one to each site of a clique might lead to more complicated scenarios on  $(p+1)$ -partite graphs. It can be shown, however, that the cavity fields can only take two different values. We conclude that at least for the case  $p \leq 2$  no extra solution appears.

For the iteration of  $x^{(0)}$  and  $x^{(1)}$  we have to distinguish two cases, represented in Fig. 4: Either the root belongs to the 1-lattice, and has only neighbors from the 0-lattice, or it belongs to the 0-lattice, and has exactly one 1-neighbor and  $p-1$  0-neighbors in each clique. The resulting equations thus read:

$$x^{(0)} = \hat{x}(x^{(1)}, \underbrace{x^{(0)}, \dots, x^{(0)}}_{p-1}, \dots) \quad (9i)$$

$$x^{(1)} = \hat{x}(\underbrace{x^{(0)}, \dots, x^{(0)}}_p, \dots), \quad (9ii)$$

where the presented block of variables has to be repeated  $k$  times in the argument of  $\hat{x}$ . The permutation symmetry of variables inside one block is already used here. The equations can be rewritten explicitly as

$$x^{(0)} = \frac{e^\mu}{(1 + x^{(1)} + (p-1)x^{(0)})^k} \quad (10i)$$

$$x^{(1)} = \frac{e^\mu}{(1 + p x^{(0)})^k}. \quad (10ii)$$

Using Eq. 8 we thus find to sub-lattice densities

$$\frac{\rho^{(0)}}{1 - \rho^{(0)}} = \frac{e^\mu}{(1 + x^{(1)} + (p-1)x^{(0)})^{k+1}} \quad (11i)$$

$$\frac{\rho^{(1)}}{1 - \rho^{(1)}} = \frac{e^\mu}{(1 + p x^{(0)})^{k+1}}. \quad (11ii)$$

Eliminating the cavity fields using Eq. (10), we find the *equilibrium equations of state* of our model:

$$e^\mu = \frac{\rho^{(0)}(1 - \rho^{(0)})^k}{(1 - \rho^{(1)} - p \rho^{(0)})^{k+1}} \quad (12i)$$

$$e^\mu = \frac{\rho^{(1)}(1 - \rho^{(1)})^k}{(1 - \rho^{(1)} - p \rho^{(0)})^{k+1}}. \quad (12ii)$$

For fixed  $k$  and  $p$ , they imply functions  $\rho^{(0)}(\mu)$  and  $\rho^{(1)}(\mu)$ . Together with the grand-canonical potential which will be calculated in the following Sec. IV B, they allow to determine the equilibrium behavior and, in particular, location and order of the crystallization transition.

Let us therefore discuss the solutions of Eqs. 12, coming first back to the liquid solution. It can be understood as the special case of equal sub-lattice densities,  $\rho^{(0)} = \rho^{(1)} = \rho$ . We thus have to solve just one global equation of state,

$$e^\mu = \frac{\rho(1-\rho)^k}{(1-(p+1)\rho)^{k+1}}. \quad (13)$$

It has just one solution, growing monotonously from  $\rho = 0$  for  $\mu \rightarrow -\infty$  to the maximally possible density  $\rho = \frac{1}{p+1}$  for  $\mu \rightarrow \infty$ .

Concentrating now on crystalline solutions with  $\rho^{(0)} \neq \rho^{(1)}$ , we find that Eqs. (12) lead to the  $p$ -independent equilibrium condition

$$\rho^{(0)}(1-\rho^{(0)})^k = \rho^{(1)}(1-\rho^{(1)})^k. \quad (14)$$

The function  $r(1-r)^k$  has a single maximum in  $r = \frac{1}{k+1}$ , thus for any  $\rho^{(1)} \neq \frac{1}{k+1}$  there is a solution for  $\rho^{(0)}$  being different from  $\rho^{(1)}$ , only for  $\rho^{(1)} = \frac{1}{k+1}$  both sub-lattice densities have to coincide. This defines a function  $\rho^{(0)} = \phi(\rho^{(1)})$ . Eqs. 12 can thus be reduced to the single equation

$$e^\mu = \frac{\rho^{(1)}(1-\rho^{(1)})^k}{(1-\rho^{(1)}-p\phi(\rho^{(1)}))^{k+1}}.$$

In order to find the spinodal point  $\mu_{sp}$ , i.e. the minimal value of  $\mu$  where the last equation has a solution, we have to minimize the right-hand side of this equation with respect to  $\rho^{(1)}$ .

For  $\rho^{(1)} \neq \frac{1}{k+1}$  this leads to a condition on the sub-lattice densities exactly at the spinodal point,

$$1 - \rho_{sp}^{(1)} - p\rho_{sp}^{(0)} - \rho_{sp}^{(0)}(k+1)((kp-1)\rho_{sp}^{(1)} - p+1) \stackrel{!}{=} 0, \quad (15)$$

which is to be completed by the equilibrium condition  $\rho_{sp}^{(0)} = \phi(\rho_{sp}^{(1)})$ . Taking as an example the case  $k = 2$ ,  $p = 2$ , there is exactly one solution to these equations:  $\rho_{sp}^{(0)} = \frac{1}{9}(6-\sqrt{33}) \simeq 0.028$  and  $\rho_{sp}^{(1)} = \frac{1}{18}(9+\sqrt{33}) \simeq 0.819$ . The global density results in  $\rho_{sp} = (p\rho_{sp}^{(0)} + \rho_{sp}^{(1)})/(p+1) \simeq 0.292$ . From Eqs. (12) we infer the chemical potential  $\mu_{sp} \simeq 2.64$  of the spinodal point. Plugging this into Eq. (13) in order to determine the liquid density at the same chemical potential, we find  $\rho_{\text{liquid}}(\mu_{sp}) \simeq 0.261$ . This value is substantially smaller than  $\rho_{sp}$ , we thus conclude that the crystalline solution appears *discontinuously* at  $\mu_{sp}$ . Note also that, for  $\mu > \mu_{sp}$  two different solutions for the sub-lattice densities are evolving, one with a monotonously increasing global density, the other one with an initially decreasing global density.

For  $\rho_{sp}^{(1)} = \frac{1}{k+1}$ , on the other hand, we know that  $\rho_{sp}^{(0)} = \phi(\rho_{sp}^{(1)}) = \frac{1}{k+1}$  coincides with  $\rho_{sp}^{(1)}$ . In this case, the crystalline solution appears *continuously* out of the liquid solution. Eqs. (12) are, however, consistent with this solution if and only if  $p = 1$ . The continuous *onset* of a crystalline solution can therefore be found only on usual Bethe-lattices. This statement does not include the scenario where an unstable crystalline solution becomes stable at  $\rho^{(0)} = \rho^{(1)} = \frac{1}{k+1}$  which will be discussed later on.

## B. The grand-canonical potential

In order to find out which of the solutions discussed above is the thermodynamically stable one, and if there are further metastable phases, we have to compare the corresponding values of the grand-canonical potential, or more precisely its density  $\omega$  per clique. Due to the distinction of the two types of vertices, we can write this as  $\omega = p\omega^{(0)} + \omega^{(1)}$ , where  $\omega^{(0/1)}$  are the potentials per 0/1-site. Knowing the cavity fields  $x^{(0)}$  and  $x^{(1)}$ ,  $\omega$  can be calculated using the following construction:

- We start with  $p(k+1)$  generalized Bethe-lattices.
- We choose one clique in each lattice, and remove all its edges.
- We obtain  $(p+1) \cdot p(k+1)$  rooted trees, among which  $p \cdot p(k+1)$  have a 0-root, and  $p(k+1)$  have a 1-root.

- We add  $p$  0-vertices, and connect each one with  $k + 1$  of the 1-trees and  $(p - 1)(k + 1)$  of the 0-trees, such that we obtain  $p$  new generalized Bethe-lattices.
- We add one 1-vertex, and connect it to the remaining  $p(k + 1)$  0-trees, such that we get one more generalized Bethe-lattice.
- In this way, we obtain  $p + 1$  lattices.

We have to sum up the changes in the grand-canonical potential induced by following the construction: We have added  $p$  0-vertices and one 1-vertex. To do so, we had to remove the edges of  $p(k + 1)$  cliques; denote the change in the potential induced by adding the edges of a clique by  $\Delta\Omega_{\text{link}}$ . Further on we had to connect the newly added vertices and the corresponding rooted trees; the change in potential induced by one of these steps is denoted by  $\Delta\Omega_{\text{site}}^{(0)}$  resp.  $\Delta\Omega_{\text{site}}^{(1)}$  according to the added vertex. The total bilance thus reads:

$$\omega = p\omega^{(0)} + \omega^{(1)} = -p(k + 1)\Delta\Omega_{\text{link}} + p\Delta\Omega_{\text{site}}^{(0)} + \Delta\Omega_{\text{site}}^{(1)}. \quad (16)$$

Using definition (2) of the grand-canonical potential, we calculate the above changes from the restricted partition functions of rooted trees:

$$\begin{aligned} e^{-\mu\Delta\Omega_{\text{link}}} &= \frac{\overbrace{\Xi_e^{(1)}(\Xi_e^{(1)})^p + \Xi_*^{(1)}(\Xi_e^{(0)})^p + p\Xi_e^{(1)}\Xi_*^{(0)}(\Xi_e^{(0)})^{p-1}}^{\text{connected rooted trees}}}{\underbrace{(\Xi_e^{(1)} + \Xi_*^{(1)})(\Xi_e^{(0)} + \Xi_*^{(0)})^p}_{\text{disconnected rooted trees}}} \\ &= \frac{1 + x^{(1)} + px^{(0)}}{(1 + x^{(1)})(1 + x^{(0)})^p}, \end{aligned} \quad (17)$$

where we have divided both numerator and denominator by  $\Xi_e^{(1)}(\Xi_e^{(0)})^p$ . Further on we get

$$\begin{aligned} e^{-\mu\Delta\Omega_{\text{site}}^{(1)}} &= \frac{\overbrace{e^\mu(\Xi_e^{(0)})^{p(k+1)} + [(\Xi_e^{(0)})^p + p\Xi_*^{(0)}(\Xi_e^{(0)})^{p-1}]^{k+1}}^{\substack{\text{1-vertex occupied} \\ \text{1-vertex empty}}}}{\underbrace{(\Xi_e^{(0)} + \Xi_*^{(0)})^{p(k+1)}}_{\text{free rooted trees}}} \\ &= \frac{e^\mu + (1 + px^{(0)})^{k+1}}{(1 + x^{(0)})^{p(k+1)}}, \end{aligned} \quad (18)$$

and

$$\begin{aligned} e^{-\mu\Delta\Omega_{\text{site}}^{(0)}} &= \frac{e^\mu[\Xi_e^{(1)}(\Xi_e^{(0)})^{p-1}]^{k+1} + [\Xi_e^{(1)}(\Xi_e^{(0)})^{p-1} + \Xi_*^{(1)}(\Xi_e^{(0)})^{p-1} + (p - 1)\Xi_e^{(1)}\Xi_*^{(0)}(\Xi_e^{(0)})^{p-2}]^{k+1}}{[(\Xi_e^{(1)} + \Xi_*^{(1)})(\Xi_e^{(0)} + \Xi_*^{(0)})^{p-1}]^{k+1}} \\ &= \frac{e^\mu + (1 + x^{(1)} + (p - 1)x^{(0)})^{k+1}}{[(1 + x^{(1)})(1 + x^{(0)})^{p-1}]^{k+1}}. \end{aligned} \quad (19)$$

This allows us to calculate the grand-canonical potential for the different crystalline and liquid solutions for the cavity fields, and thus to determine the phase diagram of the model by looking for the locally stable solution of minimal potential – provided the partitioning of the lattice in the two sublattices, i.e. the assumption of a crystalline structure, is consistent with the global structure of the lattice.

### C. The phase diagram

Let us shortly summarize the case  $p = 1$  where we have an ordinary Bethe lattice. We have found that at  $\rho_{cr} = \frac{1}{k+1}$  a crystalline solution appears continuously from the liquid one, i.e. we find a second-order crystallization transition. For  $\mu < \mu_{cr}$ , with  $\rho(\mu_{cr}) = \rho_{cr}$ , the liquid solution is the only one, and thus globally stable. For  $\mu > \mu_{cr}$ , this solution becomes locally unstable, and two stable crystalline states exist. They are connected to each other by exchanging the

two sub-lattices. For  $\mu \rightarrow \infty$ , the system approaches one of its ground states which is given by a periodic alternation of occupied and empty sites.

In the case of a generalized Bethe-lattice, i.e. for  $p > 1$ , the situation is slightly more involved. Below the spinodal point  $\mu_{sp}$  only the liquid solution exists, it thus describes the globally stable solution. It exists, however, also for larger chemical potentials and, up to  $\mu_{cr}$  (as defined in the last paragraph), it remains at least locally stable under small perturbations.

At  $\mu_{sp}$  two other, crystalline solutions appear. The first one has always  $\rho^{(1)} > \rho^{(0)}$ , and the global density is larger than the liquid one. This solution is always locally stable, as can be shown by analyzing the relaxational dynamics of the system [13]. The second crystalline solution starts with the same sub-lattice densities at the spinodal point, but its global density first decreases. In addition it is initially locally unstable, hence unphysical. At  $\mu = \mu_{cr}$ , however, both sub-lattice densities become equal,  $\rho^{(1)} = \rho^{(0)} = \frac{1}{k+1}$ , and exactly at this point it thus coincides with the liquid solution. Beyond  $\mu_{cr}$ , the new solution becomes locally stable, and thus takes over the local stability from the liquid solution. Since both  $\rho(\mu)$ -curves touch in this point with the same slope but different curvature, the corresponding transition there is of *third order*. The crystalline solution becomes also in some other aspect quite particular: The sub-lattice densities now fulfill  $\rho^{(1)} < \rho^{(0)}$ , i.e. every clique has  $p$  vertices of higher, and one vertex of lower density! Note that this transition exists only if the global density  $\frac{1}{k+1}$  can be reached. Every clique can be occupied by at most one particle, the density is thus restricted to values  $\rho < \frac{1}{p+1}$ . A necessary and sufficient condition for the existence of the inverse crystalline solution is thus given by  $k > p$ .

For all  $\mu > \mu_{sp}$  we thus find two locally stable solutions, and we have to consider the grand-canonical potentials in order to decide which solution is the globally stable one. For  $p > 1$ , the liquid solution remains the thermodynamically relevant one up to some  $\mu_s > \mu_{sp}$ , above which the first crystalline solution has the minimal  $\omega$ ; a first-order freezing transition occurs. The second crystalline solution has never the globally minimal grand-canonical potential, but it crosses the one of the liquid solution at  $\mu_{cr}$ , verifying thus the results of the local stability analysis.

It has to be remarked that in the case of ordinary Bethe-lattices, i.e.  $p = 1$ , the equations are symmetric with respect to  $\rho^{(1)}$  and  $\rho^{(0)}$ , thus normal and inverse crystallization are indistinguishable. We can therefore consider this case as a degenerate one, where the crystalline and the inverse crystalline solutions appear in the same moment, and thus  $\mu_{sp} = \mu_s = \mu_{cr}$  holds.

#### D. An example

We want to illustrate this behavior in a specific example. The system of minimal  $k$  and  $p$  showing inverse crystallization has  $k = 3$  and  $p = 2$ . We therefore concentrate on these values.

The phase diagram is shown in Fig. 5, the grand-canonical potential per clique is shown in Fig. 6. For small  $\mu$ , only the liquid phase exists. At  $\mu_{sp} \simeq 1.386$  a crystalline solution with sub-lattice densities  $\rho_{sp}^{(0)} \simeq 0.034$ ,  $\rho_{sp}^{(1)} \simeq 0.637$  and global density  $\rho_{sp} \simeq 0.235$  appears. Up to  $\mu_s \simeq 1.558$ , the liquid phase remains however the thermal equilibrium of our model. For all  $\mu$  above  $\mu_s$ , the crystalline solution of higher density becomes the globally stable one, i.e. at  $\mu_s$  the system undergoes a first-order crystallization transition. The liquid solution stays, however, also locally stable beyond  $\mu_s$ , and in absence of sufficiently strong perturbations the system remains liquid also for higher  $\mu$ . Only at  $\mu_{cr} \simeq 3.296$  it loses its local stability in a third-order transition to an inverse crystalline state with  $\rho^{(0)} > \rho^{(1)}$ . Note that the density curves of the liquid and the second crystalline solution only touch at  $\mu_{cr}$ , the inverse crystalline density is slightly larger than the liquid one, whereas the grand-canonical potentials cross each other with equal slopes.

At this point we have to remark that the entropy  $s = -\mu(\omega + \rho)$  of the inverse crystalline solution vanishes at  $\mu \simeq 5.58$ , and it becomes therefore unphysical at higher chemical potentials. Using a slight generalization of the 1RSB formalism introduced in the next section, we find for  $\mu > 5.31$  the existence of a solution that corresponds to a *crystalline glass phase* (cf. section V A 4) which seems appropriate to solve the entropy crisis. Thus, the inverse crystallization is relevant only in an interval  $\mu_{cr} < \mu < \mu_{cg}$  with  $\mu_{cg} \leq 5.31$ .

#### E. Comparison to numerical experiments

To test our analytical results on the crystallization transitions, we have performed Monte-Carlo simulations. These are naturally performed on finite lattices, and a natural finite analog of the Bethe lattice defined as an infinite tree is provided by regular random graphs. As already discussed in Sec. II, their large scale structure contains random loops which are not compatible with any division into 0- and 1-sub-lattices. This can be circumvented by imposing the consistency with the crystalline structure by generating, e.g., a random regular bipartite graph by grouping the

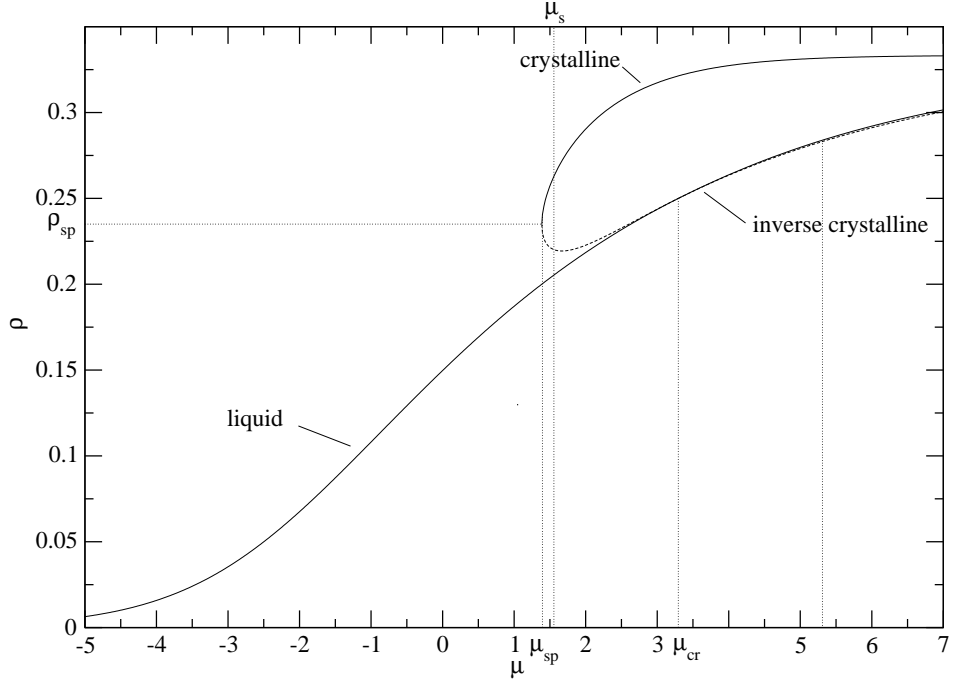


FIG. 5: Phase diagram for a generalized Bethe-lattice with  $k = 3$ ,  $p = 2$ . At  $\mu_{sp}$  a crystalline solution sets in discontinuously, and at  $\mu_s$  it becomes globally stable. At  $\mu_{cr}$  the liquid solution becomes locally unstable, and goes over into an inverse crystalline phase, which is relevant for  $\mu_{cr} < \mu < \mu_{cg}$  with  $\mu_{cg} \leq 5.31$ . Locally stable solutions are denoted by full lines, locally unstable ones by dashed lines.

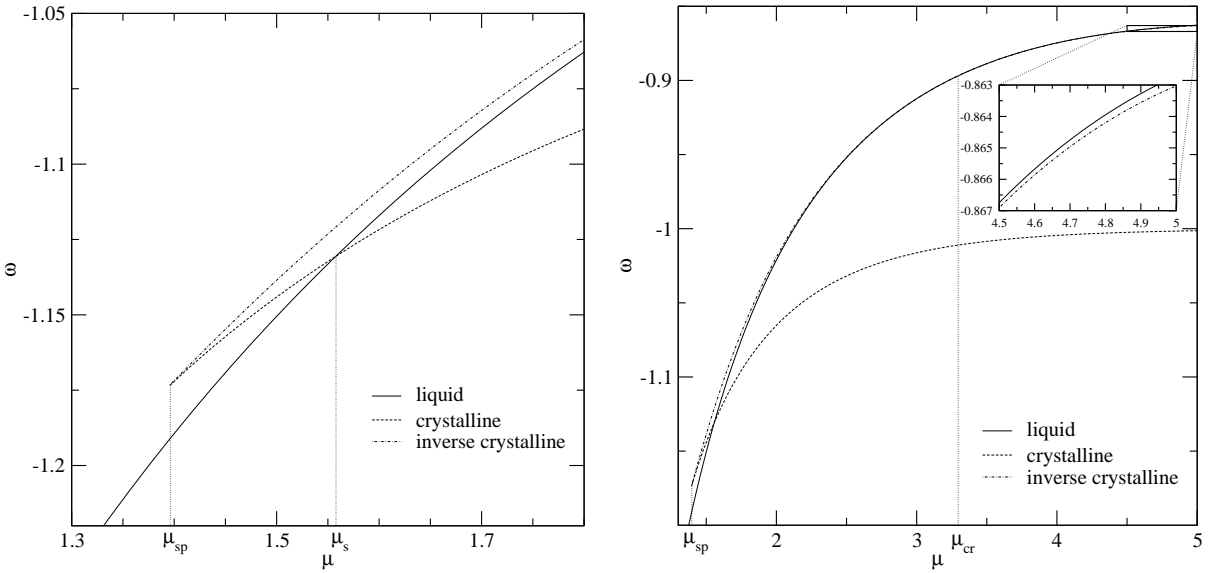


FIG. 6: Grand-canonical potential per clique  $\omega$  for  $k = 3$ ,  $p = 2$ .

vertices into two subsets of sizes  $N$  and  $pN$ , and by introducing cliques only in between one vertex from the first and  $p$  vertices from the second subset.

Note that also these graphs have an important difference to the generalized Bethe-lattices defined as infinite graphs which survives even in the thermodynamic limit: The first graphs allow only for exactly one partition into 0- and 1-lattices, whereas the second definition allows for an exponential number of such partitions. This difference is meaningful for stability properties of the system. It can be shown in numerical simulations that even when going to

$(p+1)$ -partite graphs, that allow for  $p+1$  partitions, the inverse crystalline phase becomes unstable.

In the MC simulations we have included the following microscopic processes: Particles are mobile, i.e. they are allowed to move to neighboring sites whenever these are empty and do not have further occupied neighbors (hard-core constraint), and the system is coupled to a particle bath such that particles can be generated or deleted. The rates for the last two processes have to be related by detailed balance, i.e. they have ratio  $e^\mu$ , in order to guarantee equilibration.

First, we have tested our predictions for the normal crystal phase on large graphs of  $N = 6 \cdot 10^6$  vertices. We have started the experiment in one densest packing, and then decreased the chemical potential with a rate of  $\delta\mu/\delta t = -0.2/(100 \text{ MCs})$ , and close to  $\mu_{sp}$  with  $\delta\mu/\delta t = -0.1/(200 \text{ MCs})$ , starting with  $\mu = 7$ . A further decrease in the decompactification rate did not alter the results, so we can expect thermal equilibrium. The left part of Fig. 7 shows, that the results are in perfect agreement with the analytical ones, in particular the discontinuous decrease of the density at the spinodal point is demonstrated with very high precision.

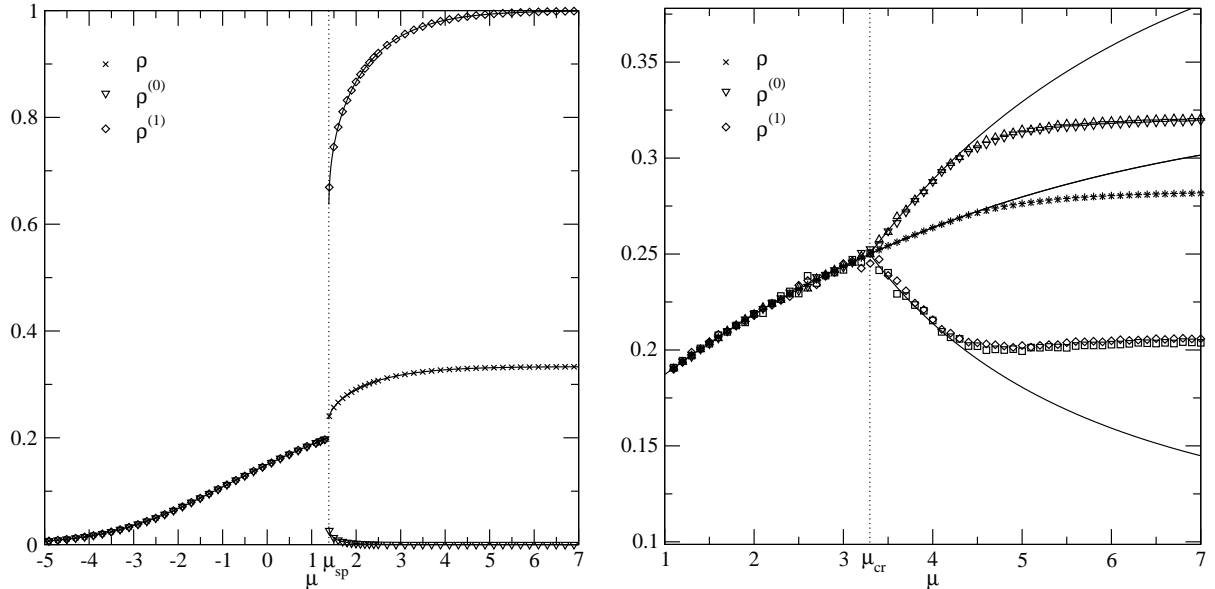


FIG. 7: Decompactification experiment for normal crystallization (left figure) and compactification experiment for inverse crystallization (right figure). Symbols which are rotated with respect to the legend correspond to smaller rates  $|\delta\mu/\delta t|$ , see main text. Analytical results are represented by full lines.

The results for the inverse crystallization were tested by starting with an empty system which was compactified in a first step to  $\mu = 1$  where only the liquid phase and no crystalline phases exist. The system was compactified by increasing  $\mu$  in discrete steps with two very small rates,  $\delta\mu/\delta t = 0, 1/(10000 \text{ MCs})$  and  $\delta\mu/\delta t = 0, 1/(5000 \text{ MCs})$ . Due to this slow dynamics we have also used a slightly smaller system of  $N = 3 \cdot 10^6$  vertices.

The results are represented in the right of Figs. 7. The first observation is that, for small  $\mu$ , numerical and analytical data coincide impressively: We find the liquid phase with equal sub-lattice densities for  $\mu < 3.3$  and a transition to the inverse crystalline phase at  $\mu_{cr} \simeq 3.3$ , as predicted in the last section. For  $\mu > \mu_{cg} \simeq 4.1$ , the results depend on the compaction rate, underlining the glassy character of the corresponding phase. It is also observed that the global density is smaller than the inverse crystalline one, which mainly results from a lower sublattice density on the 0-lattice.

We mention that besides the transition from the liquid to the inverse crystalline phase which is shown in Fig. 7 (right), there is a certain probability for the system to undergo a transition to the normal crystalline phase with  $\rho^{(1)} > \rho^{(0)}$  when compacted beyond  $\mu_{cr}$ . The dependence of this probability on the compaction rate and on the system size might be an interesting subject of further investigation.

## V. GLASSY BEHAVIOR

In the last section, we have already seen that the simple crystalline ansatz of two cavity fields  $x^{(0)}$  and  $x^{(1)}$  for solving the iterative Eq. 6 leads to inconsistencies for large  $\mu$ . The entropy of the inverse crystalline solution, which

describes a metastable phase, becomes negative at finite  $\mu$ , and the solution is not physical any more. Frequently zero-entropy points can be understood as an indicator for the existence of a glass transition at some smaller value of the chemical potential, and thus a more general solution ansatz has to be considered.

The situation is even more drastic if we consider random regular graphs as realizations of Bethe lattices. As already discussed, they are locally isomorphic to a tree, but they contain random large-scale loops which are not consistent with any crystalline structure. In particular they do not allow for a coherent partition of the original graph into two subgraphs as discussed in the context of the crystalline solution, the system is frustrated. So far, for these graphs we have only the liquid solution which, however, is in contradiction to numerical results for large  $\mu$ .

We therefore have to consider the possibility of the existence of a glassy high-density phase, or, in technical terms, we have to search for a replica symmetry broken solution (RSB). On the level of one-step RSB (1RSB) this can be achieved most easily using the cavity approach [11], as developed for finite-connectivity systems in [12], and used also in [9] for a similar lattice gas model.

We first discuss a homogeneous 1RSB solution, which is valid in particular for lattices not allowing for crystallization. At the end of this section, we also show shortly which modifications have to be made in order to account for the crystalline glass phase which was already mentioned at the end of the last section.

### A. The 1RSB cavity solution

We want to construct a non-periodic solution of Eq. (6). For small  $\mu$ , the lattice gas is very diluted, so the liquid solution is expected to be correct. For higher densities, the frustration in the systems becomes, however, relevant. In this regime, Eq. (6) is expected to have an exponential number of solutions, each one describing a thermodynamic *state* of the model. These states are, in particular, not spatially homogeneous. Let us therefore assume that the number  $\mathcal{N}_N(\omega)$  of states of density  $\omega$  of the grand-canonical potential satisfies

$$\mathcal{N}_N(\omega) \sim e^{N\Sigma(\omega)}, \quad (20)$$

where  $\Sigma(\omega) \geq 0$  is the so-called *complexity* (or *configurational entropy*). It is assumed to be a growing concave function.

We consider now a rooted tree with root  $jl$  as shown in Fig. 3 for  $j = 0, l = 0$ , and assume that the solutions for the cavity field  $x^{jl}$  and the potential  $\omega^{jl}$  are distributed according to some probability distribution  $R^{jl}(x^{jl}, \omega^{jl})$ . Repeating the iteration step represented in Fig. 3, we can calculate the distribution for the root from the distribution of the neighboring roots,

$$\begin{aligned} R^{00}(x^{00}, \omega^{00}) &= \int \prod_{j=1}^k \prod_{l=1}^p dx^{jl} d\omega^{jl} R^{jl}(x^{jl}, \omega^{jl}) \delta(x^{00} - \hat{x}(x^{11}, \dots, x^{kp})) \\ &\quad \times \delta\left(\omega^{00} - \frac{1}{N^{00}} \left( \sum_{j=1}^k \sum_{l=1}^p N^{jl} \omega^{jl} + \Delta\Omega_{\text{iter}}(x^{11}, \dots, x^{kp}) \right) \right). \end{aligned} \quad (21)$$

We have used the number  $N^{jl}$  of the vertices in the corresponding rooted tree, i.e.

$$N^{00} = \sum_{j=1}^k \sum_{l=1}^p N^{jl} + 1. \quad (22)$$

The change in the grand canonical potential is calculated via

$$\begin{aligned} e^{-\mu\Delta\Omega_{\text{iter}}} &= \frac{\text{partition function after iteration}}{\text{partition function before iteration}} \\ &= \frac{\Xi_e^{00} + \Xi_*^{00}}{\prod_{j=1}^k \prod_{l=1}^p (\Xi_e^{jl} + \Xi_*^{jl})} \\ (4) \quad &\stackrel{(4)}{=} \frac{\prod_{j=1}^k \left( \prod_{l=1}^p \Xi_e^{jl} + \sum_{l=1}^p \Xi_*^{jl} \prod_{m \neq l} \Xi_e^{jm} \right) + e^\mu \prod_{j=1}^k \prod_{l=1}^p \Xi_e^{jl}}{\prod_{j=1}^k \prod_{l=1}^p (\Xi_e^{jl} + \Xi_*^{jl})} \\ &= \frac{\prod_{j=1}^k (1 + \sum_{l=1}^p x^{jl}) + e^\mu}{\prod_{j=1}^k \prod_{l=1}^p (1 + x^{jl})}. \end{aligned} \quad (23)$$

Note that Eq. (21) assumes factorization of the *joint* distribution  $\tilde{R}(x^{11}, \omega^{11}; \dots; x^{kp}, \omega^{kp})$  of all neighbors of vertex 00. This would obviously be correct on a tree, where different rooted subtrees are disconnected and thus statistically independent. On a (generalized) random regular graph, these vertices are not the roots of  $kp$  disconnected rooted trees, so the factorization is not *a priori* true. Loops have, however, a typical length of  $\mathcal{O}(\ln N)$ , so once their short connection via vertex 00 is disregarded, they are far away. On the level of 1RSB we therefore assume that the joint distribution factorizes, and we can use Eq. (21).

On these graphs, regular structures like a crystalline one are forbidden by the existence of random loops. We therefore assume homogeneity on the level of the field distributions,  $R^{00} \equiv R^{11} \equiv \dots \equiv R^{kp} \equiv R$ , thus Eq. 21 becomes a self-consistent equation for  $R(x, \omega)$ . In order to solve this equation, we use assumption (20) and write

$$R(x, \omega) \sim e^{N\Sigma(\omega)} P^{(\omega)}(x), \quad \text{with} \quad \int dx P^{(\omega)}(x) = 1, \quad (24)$$

where  $P^{(\omega)}$  is the distribution of cavity fields with fixed  $\omega$ . In order to derive an equation for this function, we fix the density of the grand-canonical potential at some arbitrary value  $\omega_0$ , and introduce the parameter

$$m(\omega_0) \doteq \frac{1}{\mu} \frac{d\Sigma}{d\omega}(\omega_0) \quad (25)$$

and linearize the complexity in a small vicinity  $\mathcal{V}_{\omega_0}$  of  $\omega_0$ :

$$\Sigma(\omega) \simeq \Sigma(\omega_0) + m\mu(\omega - \omega_0). \quad (26)$$

Since  $\Sigma$  was assumed to be concave, there is a one-to-one correspondence between  $\omega_0$  and  $m$ . We define the distribution

$$P^{(m)}(x) = \frac{1}{|\mathcal{V}_{\omega_0}|} \int_{\omega \in \mathcal{V}_{\omega_0}} d\omega P^{(\omega)}(x). \quad (27)$$

Plugging this into Eq. (21), we find in the limit of a vanishing vicinity  $\mathcal{V}_{\omega_0}$  the self-consistent equation

$$P^{(m)}(x) \propto \int \prod_{j=1}^k \prod_{l=1}^p dx^{jl} P^{(m)}(x^{jl}) \delta(x - \hat{x}(x^{11}, \dots, x^{kp})) e^{-m\mu\Delta\Omega_{\text{iter}}(x^{11}, \dots, x^{kp})} \quad (28)$$

which is called the *factorized 1RSB cavity equation* for the cavity field distribution in our hard-sphere lattice gas model.

To clarify the meaning of  $m$ , we calculate

$$\Xi(m) = \sum_{\alpha} e^{-Nm\mu\omega^{(\alpha)}} = \int d\omega \mathcal{N}_N(\omega) e^{-Nm\mu\omega} \sim \int d\omega e^{N(\Sigma(\omega) - m\mu\omega)} = e^{-Nm\mu\Phi(m)} \quad (29)$$

with the sum running over all states  $\alpha$ , i.e. over all solutions of Eq. (6). Note that, for  $m = 1$ , this reproduces the grand-canonical partition function. In the thermodynamic limit,  $\Phi(m)$  is given by the saddle-point approximation,

$$\Phi(m) = \omega - \frac{1}{m\mu} \Sigma(\omega), \quad \text{with} \quad \partial_{\omega} \Sigma(\omega) = m\mu, \quad (30)$$

which reproduces the definition of  $m(\omega)$  in Eq. (25). From Eq. (30) follows that

$$\partial_m \Phi(m) = \partial_m \omega + \frac{1}{m^2 \mu} \Sigma(\omega) - \frac{1}{m\mu} \partial_{\omega} \Sigma(\omega) \partial_m \omega = \frac{1}{m^2 \mu} \Sigma(\omega). \quad (31)$$

Let us compare Eq. (30) with the usual equation for the entropy

$$\Phi(m) = \omega - \frac{1}{m\mu} \Sigma(\omega) \quad \text{and} \quad \omega = -\rho - \frac{1}{\mu} s. \quad (32)$$

There is an obvious similarity: As  $s$  counts the number of microscopic configurations,  $\Sigma$  counts the number of states. As  $\mu$  serves as a control parameter selecting configurations of a given density  $\rho$ , the parameter  $m$  allows to focus on states of arbitrarily given  $\omega$ . Therefore  $\Phi(m)$  plays, on the level of states, the same role as the grand-canonical

potential on the level of configurations. Following this analogy, we can calculate  $\Phi(m)$  as done in Sec. IV B for the grand-canonical potential:

$$\Phi(m) = -\frac{p(k+1)}{p+1} \Delta\Phi_{\text{link}}(m) + \Delta\Phi_{\text{site}}(m) \quad (33)$$

with

$$e^{-m\mu\Delta\Phi_{\text{site}}} = \int \prod_{j=1}^{k+1} \prod_{l=1}^p dx^{jl} P(x^{jl}) e^{-m\mu\Delta\Omega_{\text{site}}(x^{11}, \dots, x^{k+1,p})} \quad (34)$$

and

$$e^{-m\mu\Delta\Phi_{\text{link}}} = \int \prod_{l=1}^{p+1} dx^{(l)} P(x^{(l)}) e^{-m\mu\Delta\Omega_{\text{link}}(x^{(1)}, \dots, x^{(p+1)})} . \quad (35)$$

$\Delta\Omega_{\text{site}}$  and  $\Delta\Omega_{\text{link}}$  are the direct generalizations of the corresponding quantities in Sec. IV B:

$$e^{-\mu\Delta\Omega_{\text{link}}} = \frac{1 + \sum_{l=1}^{p+1} x^{(l)}}{\prod_{l=1}^{p+1} (1 + x^{(l)})}, \quad e^{-\mu\Delta\Omega_{\text{site}}} = \frac{e^\mu + \prod_{j=1}^{k+1} (1 + \sum_{l=1}^p x^{jl})}{\prod_{j=1}^{k+1} \prod_{l=1}^p (1 + x^{jl})} . \quad (36)$$

### 1. Static and dynamic glass transition

Let us consider the 1RSB equation (28) first for  $m = 1$ . As already mentioned,  $\Xi(m = 1)$  then gives the usual partition function,

$$\Xi(\mu) \sim \int d\omega e^{N(\Sigma(\omega) - \mu\omega)}, \quad (37)$$

where the integration runs over the interval  $(\omega_{\min}, \omega_{\max})$  with positive  $\Sigma(\omega)$ .

Let us first discuss the case  $p > 1$ . For small  $\mu$ , Eq. (28) has only the liquid solution  $P(x) = \delta(x - x^*)$ . The particle density is low enough that the frustration resulting from long loops is not relevant. At some chemical potential  $\mu = \mu_d$ , the first non-trivial solution appears discontinuously. This point is called the *dynamical glass transition*. For  $\mu > \mu_d$  the system has exponentially many states, the complexity  $\Sigma(\omega_s) > 0$  is positive. The grand-canonical potential  $\omega_s$  of one state can be calculated via the saddle point method from Eq. (37), i.e. as a solution of  $\mu = \partial_\omega \Sigma(\omega)$ . The potential  $\omega^*$  of the liquid solution is given by  $\omega^* = \Phi(m = 1)$ . With Eq. (30) we conclude  $\omega_s > \omega^*$ . The states born at  $\mu_d$  are therefore metastable ones, the thermodynamically stable solution remains still the liquid one. The dynamics of the system becomes, however, trapped already at  $\mu_d$  by the exponential number of metastable states, i.e. the system remains dynamically out of equilibrium, cf. the discussion in [15].

Increasing  $\mu$  beyond  $\mu_d$ , the complexity  $\Sigma(\omega_s)$  decreases, until it vanishes at  $\mu = \mu_s$ . According to Eq. (30), the grand-canonical potential  $\omega_s$  of the 1RSB solution equals here the one of the liquid solution, and  $\mu = \mu_s$  indicates thus the location of a *static*, i.e. thermodynamic glass transition.

For  $\mu > \mu_s$  the naive application of the saddle-point method leads to an unphysical solution  $\omega_s < \omega_{\min}$  of negative complexity. The correct exponentially dominating contribution in Eq. (37) is thus given at the interval limit  $\omega_s = \omega_{\min}$ . In this situation we need a “corrected” saddle-point equation  $m\mu = \partial_\omega \Sigma(\omega)$  (cf. Eq. (30)), which defines the value  $m_s = \frac{1}{\mu} \partial_\omega \Sigma(\omega = \omega_s)$ . According to Eq. (30) we thus obtain the grand-canonical potential of the 1RSB equilibrium via  $\Phi(m_s) = \omega_s = \omega_{\min}$ . Using  $\Sigma(\omega_s) = \Sigma(\omega_{\min}) = 0$  and Eq. (31) we thus find

$$\partial_m \Phi(m = m_s) = 0 . \quad (38)$$

Also other values of  $m$  have a physical significance. For  $m < m_s$  we get metastable states with  $\omega > \omega_s$ . These are important for understanding the dynamics of the system. A particular importance has here the value  $\omega_d$  where the complexity is maximized, cf. Sec VI. Larger values  $m > m_s$  lead to negative complexity which can be reinterpreted in the context of atypical graphs - their complexity corresponds to the probability that a (generalized) random regular graph has states of this smaller grand-canonical potential. An example for such an untypical graph is the multi-partite one allowing for a crystalline solution as discussed before.

The situation is easier for  $p = 1$ , i.e. for standard Bethe lattices. Here  $\mu_d$  and  $\mu_s$  coincide and mark a continuous spin-glass transition. The region, where the dynamics is dominated by an exponential number of metastable states, disappears.

## 2. The spin-glass instability of the liquid solution

An upper bound for  $\mu_d$  is given by the spin-glass instability of the liquid solution. This instability means that a small perturbation of  $x^*$  is amplified during the iteration of Eq. (28). The criterion for the instability is

$$kp \left| \frac{\partial \hat{x}(x^*, \dots, x^*)}{\partial x^{11}} \right|^2 > 1. \quad (39)$$

Equality holds at critical values  $\mu_g$  of the chemical potential, and  $\rho_g$  of the density. According to Eq. (6) this happens at

$$\rho_g = \frac{1}{\sqrt{kp} + 1}. \quad (40)$$

Above this point, the liquid solution is locally unstable.

For  $p = 1$ , also this instability coincides with  $\mu_d$  and  $\mu_s$ .

## 3. Solving the 1RSB equation via population dynamics

Solving Eq. (28) seems to be too complicated, we therefore have to solve it numerically. The main idea hereby is to iterate the self-consistency equation until a fixed point is reached. This happens by representing first  $P^{(m)}$  by a finite but large population  $\{x_1, \dots, x_M\}$ ,  $M \gg 1$  of cavity fields, and by updating this population via a population dynamical algorithm [12]: In every step  $kp$  fields are selected randomly from the population, and a new field is calculated by  $\hat{x}$ . This field replaces one or more of the old fields in the population, where the number of substituted fields is a function of the reweighting factor in Eq. (28).

For our example  $k = 3$ ,  $p = 2$ , we find the following results: From Eq. (40) we conclude that  $\rho_g = \frac{1}{\sqrt{6}+1} \simeq 0.290$ . It is, in particular, larger than  $\rho_{\text{krit}} = \frac{1}{k+1} = 0.25$ , which is true for all  $k > p$ . With Eq. 13 we find  $\mu_g \simeq 5.89$ , this value is confirmed by the population-dynamical algorithm.

Further on, we find that at  $\mu_d \simeq 4.85$  the first non-trivial solution for  $P^{(m)}$  emerges discontinuously. In principle also the static spin-glass transition  $\mu_s$  can be determined by the population-dynamical algorithm. The problem is, however, that it results from a comparison of the grand-canonical potentials of the liquid and the glassy solutions, which are subject to large fluctuations. Even a large statistics allows only for a rough estimate of  $\mu_s \simeq 5.0$ .

Note that, for the case considered here, the dynamical and the static RSB transition are located beyond the inverse-crystallization point, where the liquid solution becomes locally unstable. It is, however, possible to validate the correctness of the result by numerical simulations which have to be performed on a (generalized) random regular graph. These graphs have a large-scale loop structure which is not consistent with any crystalline packing, cf. the discussion in Sec. II, and thus the system undergoes directly the glass transition if compactified until  $\mu_d$ . As can be seen in Fig. 8, the compaction dynamics falls out of equilibrium even before the dynamical glass transition, but slower and slower compaction allows for a closer approach to  $\mu_d$ , showing thus the compaction-rate effects which are typical for glass formers.

## 4. Glass-instability of the inverse crystalline phase ( $k = 3$ , $p = 2$ )

A stability analysis of the inverse crystalline phase toward a 1RSB “glassy” phase requires to embed the inverse crystalline solution in the 1RSB formalism. To this purpose we rewrite the 1RSB equation (28) without assuming homogeneity of the field distributions  $P^{00}, P^{11}, \dots, P^{kp}$ :

$$P^{00}(x) \propto \mathcal{F}[P^{11}, \dots, P^{kp}](x) \quad (41)$$

where  $\mathcal{F}$  contains the r.h.s. of the 1RSB equation. The dependence on  $m$  is eliminated by putting  $m \doteq 1$  which can be justified as we are only interested in transitions points to the glassy phase. The canonical embedding now reads

$$P^{(0)} \propto \mathcal{F}[P^{(1)}, P^{(0)}, \dots, P^{(0)}; \dots], \quad P^{(1)} \propto \mathcal{F}[P^{(0)}, \dots, P^{(0)}; \dots], \quad (42)$$

where the displayed blocks in the argument of  $\mathcal{F}$  must be repeated  $k$  times similar to Eq. (9). The distributions  $P^{(0)}$  and  $P^{(1)}$  are simply  $\delta$ -functions at the values  $x^{(0)}$  and  $x^{(1)}$  of the local fields according to the inverse crystalline solution. The local instability of the iteration defined by Eq. (42) can be detected by evaluating  $\mathcal{F}$  for  $P^{(0)}$  and  $P^{(1)}$

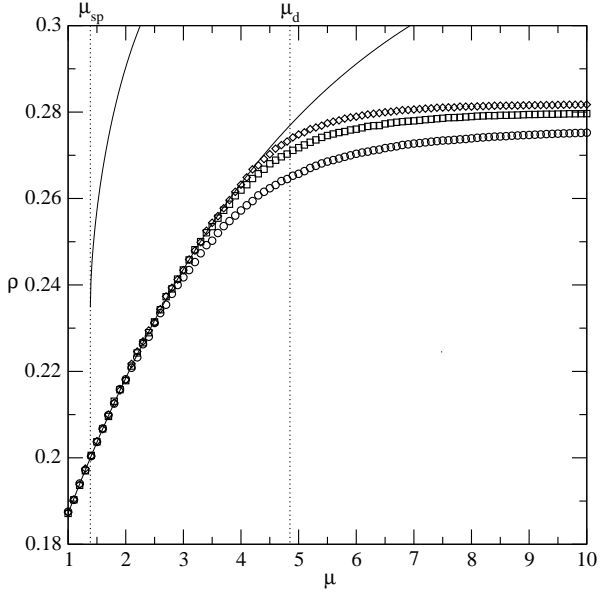


FIG. 8: Compactification experiments for a generalized random regular graph  $k = 3$ ,  $p = 2$ , and  $N = 450000$  sites. The full lines give the analytical results for the liquid and crystalline densities, whereas the symbols correspond to compaction rates  $\delta\mu/\delta t = 0.1/10$  MCs (circles),  $0.1/100$  MCs (squares) and  $0.1/1000$  MCs (diamonds). Obviously, the systems falls out of the liquid equilibrium when the equilibration time starts to exceed the waiting time at the corresponding chemical potential, i.e. before the latter reaches  $\mu_d$ .

chosen as Gaussian distributions with respective variances  $\varepsilon^{(0)}$  and  $\varepsilon^{(1)}$ . Under neglecting of the reweighting factors in  $\mathcal{F}$  one easily calculates the variances  $\varepsilon^{(0)'} \text{ and } \varepsilon^{(1)'}$  after one step of the iteration:

$$\begin{aligned} \varepsilon^{(0)'} &= \sqrt{k(p-1) \left| \frac{\partial \hat{x}(x^{(1)}, x^{(0)}, \dots, x^{(0)}; \dots)}{\partial x^{12}} \right|^2 \varepsilon^{(0)2} + k \left| \frac{\partial \hat{x}(x^{(1)}, x^{(0)}, \dots, x^{(0)}; \dots)}{\partial x^{11}} \right|^2 \varepsilon^{(1)2}} \\ \varepsilon^{(1)'} &= \sqrt{kp} \left| \frac{\partial \hat{x}(x^{(0)}, \dots, x^{(0)}; \dots)}{\partial x^{11}} \right| \varepsilon^{(0)}. \end{aligned} \quad (43)$$

We note that the equations deliver precisely the spin-glass instability of the liquid solution when we choose all local fields equal to  $x^*$ . In the case of local fields  $x^{(0)}$  and  $x^{(1)}$  a stability criterion can be derived by evaluating the eigenvalues of the Jacobian matrix attributed to the iteration defined by Eq. (43). We find that for the inverse crystalline solution  $\varepsilon^{(0)} = \varepsilon^{(1)} = 0$  is a stable fixed point of the iteration only if  $\mu < \mu_{g,inv} \simeq 5.31$  which is smaller than  $\mu_g \simeq 5.89$ . We can check this result via population dynamics where we encode the distributions  $P^{(0)}$  and  $P^{(1)}$  using two populations of fields. It turns out that the local instability  $\mu_{g,inv}$  is exact and furthermore we can show that for  $\mu < \mu_{g,inv}$  only the trivial field distributions corresponding to the crystalline and inverse crystalline solutions solve the 1RSB equations (42). This is obviously in contradiction with the results from section IV E where the existence of a glassy crystalline phase is shown for  $\mu > \mu_{cg} \simeq 4.1$ . We can thus conclude that the 1RSB formalism is not sufficient to describe the onset of a glassy phase.

A way out of this dilemma might consist in passing to a description in 2RSB which would mean to work with two distributions of field distributions attributed to the sub-lattices. A 2RSB treatment of the problem seems, however, complicated to handle. For the moment, the construction of a “glassy” solution which would illuminate the discrepancy between  $\mu_{g,inv}$  and  $\mu_{cg}$  remains an open problem.

## VI. CLOSE-PACKING LIMIT ( $\mu \rightarrow \infty$ )

The 1RSB solution developed in the preceding section V A cannot be calculated analytically in the case of general  $\mu$  where a solution is obtained by a numerical method (population dynamics).

For the limiting case  $\mu \rightarrow \infty$  which corresponds to a close-packing, however, one can easily show that the transformed

local fields

$$h^{jl} = \frac{1}{\mu} \ln(x^{jl} + 1) = \frac{1}{\mu} \ln \left( \frac{\Xi_e^{jl} + \Xi_*^{jl}}{\Xi_e^{jl}} \right) \quad (44)$$

must have a particularly simple distribution in the 1RSB formalism which enables us to undertake an explicit calculation.

We first note that for  $\mu \rightarrow \infty$  the grand-canonical partition function is dominated by the terms that correspond to configurations with a maximal number  $N_{e/*}^{jl}$  of particles, *i.e.*  $\Xi_{e/*}^{jl} \propto e^{\mu N_{e/*}^{jl}}$  asymptotically with a factor that counts the number of close-packings and does not depend on  $\mu$ . This in mind, we find that Eq. 44 becomes

$$h^{jl} = \max(N_e^{jl}, N_*^{jl}) - N_e^{jl} \quad (45)$$

which implies that the local fields  $h^{jl}$  must be nonnegative integer numbers.

Using again the properties of the partition function for  $\mu \rightarrow \infty$  we can also rewrite the iteration equations 4 in terms of maximal numbers of particles:

$$N_e^{00} = \sum_{j=1}^k \max \left( \sum_{l=1}^p N_e^{jl}, \left\{ N_*^{jl} + \sum_{\substack{m=1 \\ m \neq l}}^p N_e^{jm} \mid l = 1, \dots, p \right\} \right) \quad (46)$$

$$N_*^{00} = 1 + \sum_{j=1}^k \sum_{l=1}^p N_e^{jl}. \quad (47)$$

We use these relations to determine the maximal value of  $h^{jl}$ , putting  $j = 0$  and  $l = 0$  without loss of generality. Following (45) the interesting case is  $N_*^{00} > N_e^{00}$  where we find

$$\begin{aligned} h^{00} &= N_*^{00} - N_e^{00} \\ &= 1 - \left( \sum_{j=1}^k \max \left( \sum_{l=1}^p N_e^{jl}, \left\{ N_*^{jl} + \sum_{\substack{m=1 \\ m \neq l}}^p N_e^{jm} \mid l = 1, \dots, p \right\} \right) - \sum_{j=1}^k \sum_{l=1}^p N_e^{jl} \right) \\ &= 1 - \sum_{j=1}^k \max \left( 0, \{N_*^{jl} - N_e^{jl} \mid l = 1, \dots, p\} \right) \end{aligned}$$

which implies  $h^{00} \leq 1$ . Thus we have shown that the transformed local fields  $h^{jl}$  satisfy  $h^{jl} \in \{0, 1\}$ .

This result, which shows the interest of working with  $h^{jl}$  instead of  $x^{jl}$ , enables us to reduce drastically the degrees of freedom in the 1RSB field distribution by making a simple one-parameter ansatz:

$$P(h) = p_0 \delta(h) + p_1 \delta(h-1) \quad (48)$$

where normalization requires  $p_0 + p_1 = 1$ .

The pair of parameters  $p_0, p_1$  must be chosen such that the ansatz solves the 1RSB cavity equation (28) which can be directly rewritten for the transformed local fields:

$$P^{(m)}(h^{00}) \propto \int \prod_{j=1}^k \prod_{l=1}^p dh^{jl} P^{(m)}(h^{jl}) \delta(h^{00} - \hat{h}(h^{11}, \dots, h^{kp})) e^{-m\mu \Delta \Omega_{\text{iter}}(h^{11}, \dots, h^{kp})}, \quad (49)$$

where the recursion relation  $\hat{h}$  of the local fields and the change in the grand-canonical potential  $\Delta \Omega_{\text{iter}}$  per iteration step are now given by

$$e^{\mu \hat{h}(h^{11}, \dots, h^{kp})} = 1 + \frac{e^\mu}{\prod_{j=1}^k (1 - p + \sum_{l=1}^p e^{\mu h^{jl}})} \quad (50)$$

and

$$e^{-\mu \Delta \Omega_{\text{iter}}(h^{11}, \dots, h^{kp})} = \frac{\prod_{j=1}^k (1 - p + \sum_{l=1}^p e^{\mu h^{jl}}) + e^\mu}{\prod_{j=1}^k \prod_{l=1}^p e^{\mu h^{jl}}} \quad (51)$$

as follows directly from Eq. (6) and Eq. (23).

For practical reasons we define a vector  $\vec{\nu}$  with  $k$  components that encodes the relevant information of a local field configuration  $\{h^{11}, \dots, h^{kp}\}$ :

$$\nu_j \doteq \sum_{l=1}^p h^{jl}. \quad (52)$$

As  $h^{jl}$  satisfies  $h^{jl} \in \{0, 1\}$ ,  $\nu_j$  counts the non-vanishing fields in the  $j$ th clique. Furthermore we define a norm by

$$|\vec{\nu}| \doteq \#\{\nu_j \neq 0 \mid j = 1, \dots, k\}. \quad (53)$$

We can see from Eq. (50) and Eq. (51) that  $\hat{h}$  and  $\Delta\Omega_{\text{iter}}$  are functions of  $\vec{\nu}$  only. We calculate these quantities explicitly:

$$\begin{aligned} \hat{h} &= \frac{1}{\mu} \ln \left( 1 + \frac{e^\mu}{\prod_{j=1}^k (1 - p + \sum_{l=1}^p e^{\mu h^{jl}})} \right) \\ &= \frac{1}{\mu} \ln \left( 1 + \frac{e^\mu}{\prod_{j=1}^k (1 - \nu_j + \nu_j e^\mu)} \right) \\ &\stackrel{\mu \rightarrow \infty}{=} \begin{cases} 1 & \text{if } |\vec{\nu}| = 0 \\ 0 & \text{if } |\vec{\nu}| > 0 \end{cases} \end{aligned} \quad (54)$$

and

$$\begin{aligned} \Delta\Omega_{\text{iter}} &= \frac{1}{\mu} \ln \left( \frac{\prod_{j=1}^k \prod_{l=1}^p e^{\mu h^{jl}}}{\prod_{j=1}^k (1 - p + \sum_{l=1}^p e^{\mu h^{jl}}) + e^\mu} \right) \\ &= \sum_{j=1}^k \sum_{l=1}^p h^{jl} - \frac{1}{\mu} \ln \left( \prod_{j=1}^k \left( 1 - p + \sum_{l=1}^p e^{\mu h^{jl}} \right) + e^\mu \right) \\ &= \sum_{j=1}^k \nu_j - \frac{1}{\mu} \ln \left( \prod_{j=1}^k (1 - \nu_j + \nu_j e^\mu) + e^\mu \right) \\ &\stackrel{\mu \rightarrow \infty}{=} \begin{cases} -1 & \text{if } |\vec{\nu}| = 0 \\ \sum_{j=1}^k \nu_j - |\vec{\nu}| \\ = \sum_{j=1}^k \max(0, \nu_j - 1) \\ = \sum_{j=1}^k \max(1, \nu_j) - k & \text{if } |\vec{\nu}| > 0 \end{cases} \end{aligned} \quad (55)$$

These results permit us to evaluate the 1RSB Eq. (49) for the ansatz (48) as they reduce the integrations in the equation to a simple combinatoric problem.

We see from Eq. (54) that only the configuration  $\vec{\nu} = \vec{0}$  contributes to  $h^{00} = 1$ . With the ansatz for  $P(h)$  we deduce immediately from the 1RSB equation that

$$p_1 \propto p_0^{kp} e^y \quad (56)$$

holds, where we have set  $y \doteq m\mu$  and used  $\Delta\Omega_{\text{iter}}$  from Eq. (55).

In a second step we must sum up the contributions to  $h^{00} = 0$  that come from all configurations with  $\vec{\nu} \neq \vec{0}$ . To this purpose we note that there are

$$\prod_{j=1}^k \binom{p}{\nu_j}$$

different realizations of a configuration  $\vec{\nu}$  with fields  $\{h^{11}, \dots, h^{kp}\}$ .

For each configuration we collect the probabilities emerging from the ansatz yielding a factor

$$p_1^{\sum_{j=1}^k \nu_j} p_0^{kp - \sum_{j=1}^k \nu_j}.$$

In addition, we have to take into account the reweighting factor

$$e^{-y\Delta\Omega_{\text{iter}}} = e^{yk} e^{-y\sum_{j=1}^k \max(1, \nu_j)}.$$

We obtain the contribution from a configuration  $\vec{\nu} \neq \vec{0}$  by taking the product of the three terms

$$\prod_{j=1}^k \left\{ \binom{p}{\nu_j} p_1^{\nu_j} p_0^{p-\nu_j} e^y e^{-y \max(1, \nu_j)} \right\}.$$

The overall contribution to  $h^{00} = 0$  can now be calculated by summation over the components of  $\vec{\nu} \neq \vec{0}$ :

$$\begin{aligned} p_0 &\propto \sum_{\nu_1=0}^p \cdots \sum_{\nu_k=0}^p \prod_{j=1}^k \left\{ \binom{p}{\nu_j} p_1^{\nu_j} p_0^{p-\nu_j} e^y e^{-y \max(1, \nu_j)} \right\} \underbrace{- p_0^{kp}}_{\substack{\text{correction for} \\ \nu_1=\cdots=\nu_k=0}} \\ &= \prod_{j=1}^k \left\{ \sum_{\nu_j=0}^p \binom{p}{\nu_j} p_1^{\nu_j} p_0^{p-\nu_j} e^y e^{-y \max(1, \nu_j)} \right\} - p_0^{kp} \\ &= \left\{ e^y (p_1 e^{-y} + p_0)^p \underbrace{- e^y p_0^p + p_0^p}_{\substack{\text{correction for} \\ \nu_j=0}} \right\}^k - p_0^{kp}. \end{aligned} \quad (57)$$

Making use of normalization ( $p_0 + p_1 = 1$ ) we end up with the iterative equations for the probabilities  $p_0$  and  $p_1$ :

$$\hat{p}_0(p_0, p_1) = \frac{\{e^y (p_1 e^{-y} + p_0)^p - p_0^p (e^y - 1)\}^k - p_0^{kp}}{\{e^y (p_1 e^{-y} + p_0)^p - p_0^p (e^y - 1)\}^k + p_0^{kp} (e^y - 1)} \quad (58\text{i})$$

$$\hat{p}_1(p_0, p_1) = \frac{p_0^{kp} e^y}{\{e^y (p_1 e^{-y} + p_0)^p - p_0^p (e^y - 1)\}^k + p_0^{kp} (e^y - 1)}. \quad (58\text{ii})$$

The equations can be solved numerically for given  $y$  with the help of a computer algebra system.

It remains the question which value  $y = y_s$  we must choose in order to describe thermodynamic equilibrium. The answer is given in section V A via the condition that the configurational entropy must vanish, *i.e.*  $\Sigma(y_s) = 0$ . We use Eq. 31 with the substitution  $y = m\mu$  to find

$$\Sigma(y) = y^2 \partial_y \Phi(y). \quad (59)$$

which provides  $\partial_y \Phi(y = y_s) = 0$  as an alternative condition for  $y_s$ .

Consequently, we shall compute  $\Phi(y)$  to complete the picture of the close-packing limit.  $\Phi(y)$  is given by Eq. (33) with Eq. (34) and (34) as well as Eq. (36). We proceed analogously to the derivation of the equations for  $p_0, p_1$ : in a first step, we evaluate Eq. (36) with transformed local fields in the limit  $\mu \rightarrow \infty$ . In a second step, the integrations in Eq. (34) and (34) are performed. This reads:

$$\begin{aligned} \Delta\Omega_{\text{link}} &= \sum_{l=1}^{p+1} h^{(l)} - \frac{1}{\mu} \ln \left( \sum_{l=1}^{p+1} e^{\mu h^{(l)}} - p \right) \\ &= \nu - \frac{1}{\mu} \ln(1 - \nu + \nu e^\mu) \\ &\stackrel{\mu \rightarrow \infty}{=} \begin{cases} 0 & \text{if } \nu = 0 \\ \nu - 1 & \text{if } \nu > 0 \end{cases}, \end{aligned} \quad (60)$$

where we have set  $\nu \doteq \sum_{l=1}^{p+1} h^{(l)}$ . Further on we have

$$\begin{aligned}
\Delta\Omega_{\text{site}} &= \sum_{j=1}^{k+1} \sum_{l=1}^p h^{jl} - \frac{1}{\mu} \ln \left( \prod_{j=1}^{k+1} \left( 1 - p + \sum_{l=1}^p e^{\mu h^{jl}} \right) + e^\mu \right) \\
&= \sum_{j=1}^{k+1} \nu_j - \frac{1}{\mu} \ln \left( \prod_{j=1}^{k+1} (1 - \nu_j + \nu_j e^\mu) + e^\mu \right) \\
&\stackrel{\mu \rightarrow \infty}{=} \begin{cases} -1 & \text{if } |\vec{\nu}| = 0 \\ \sum_{j=1}^{k+1} \max(1, \nu_j) - (k+1) & \text{if } |\vec{\nu}| > 0 \end{cases}. \tag{61}
\end{aligned}$$

Note that the expression for  $\Delta\Omega_{\text{site}}$  is obtained from  $\Delta\Omega_{\text{iter}}$  by the substitution  $k \rightarrow k+1$ . We perform the integrations to obtain

$$\begin{aligned}
e^{-y\Delta\Phi_{\text{link}}} &= p_0^{p+1} e^{-y \cdot 0} + \sum_{\nu=1}^{p+1} \binom{p+1}{\nu} p_1^\nu p_0^{p+1-\nu} e^{-y \cdot (\nu-1)} \\
&= e^y (p_1 e^{-y} + p_0)^{p+1} - p_0^{p+1} (e^y - 1) \tag{62}
\end{aligned}$$

$$\text{and } e^{-y\Delta\Phi_{\text{site}}} = \{e^y (p_1 e^{-y} + p_0)^p - p_0^p (e^y - 1)\}^{k+1} + p_0^{(k+1)p} (e^y - 1), \tag{63}$$

where the latter term also results from the sum of the contributions (56) and (57) after substituting  $k \rightarrow k+1$ .

The knowledge of  $\Phi(y)$  can serve to access the particle density  $\rho$ :

$$\rho = \partial_\mu \ln \Xi = -\partial_\mu (\mu \Phi) = -\partial_y (y \Phi). \tag{64}$$

Specially in thermodynamic equilibrium the particle density is given by

$$\rho_s = \rho(y_s) = -\Phi(y_s), \tag{65}$$

as  $\partial_y \Phi$  vanishes at  $y_s$ .

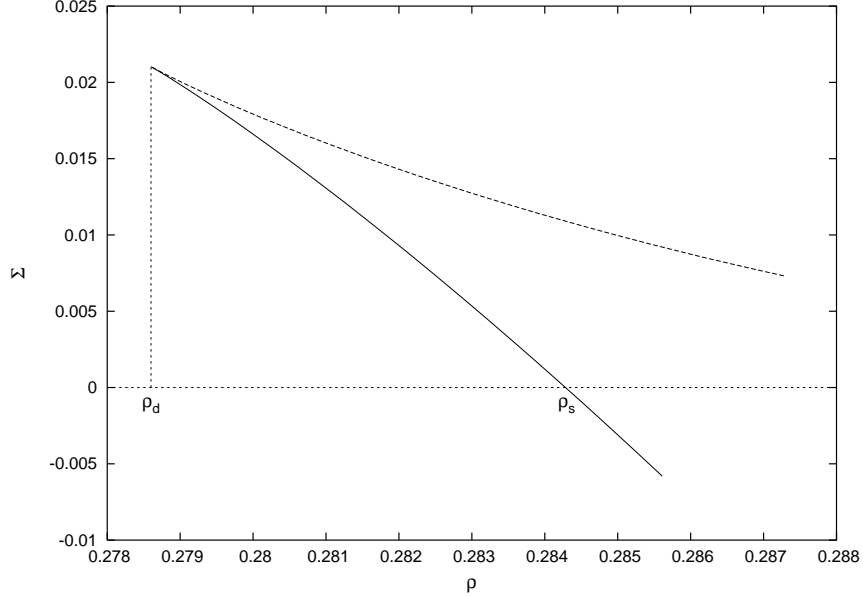


FIG. 9: 1RSB solution for the complexity  $\Sigma$  as a function of the particle density  $\rho$  in the limit  $\mu \rightarrow \infty$  ( $k = 3, p = 2$ ).  $\Sigma$  being a concave function, only the full line has physical meaning.  $\Sigma < 0$  is attributed to untypical graphs that have vanishing statistical weight.

Eq. (64) together with Eq. (59) deliver the complexity  $\Sigma(\rho)$  as a curve parameterized by  $y$  (Fig. 9). The complexity  $\Sigma$  has a maximum at  $\rho_d < \rho_s$  while it vanishes for the equilibrium density  $\rho_s$ . The meaning of  $\rho_d$  for the dynamics of the system, in particular for dynamics induced by local algorithms, is discussed in the subsequent section.

Some results for the particle density of a close-packing  $\rho_\infty \equiv \rho_s$  and the density  $\rho_d$  with maximal complexity as obtained in the 1RSB solution are shown for different  $k$  and  $p$  in Fig. 10.

### A. Comparison with numerical bounds

We have compared the analytical 1RSB results for  $\rho_\infty$  and  $\rho_d$  with numerical lower bounds for  $\rho_\infty$  that were obtained in Monte-Carlo simulations. For given  $k$  and  $p$  random graphs of size  $N = (p + 1) \cdot 500\,000$  that have locally the structure of a generalized Bethe lattice were generated. Roughly speaking, this can be achieved by iterating the following procedure until every vertex has  $(k + 1)p$  neighbors: choose randomly  $p + 1$  vertices with less than  $(k + 1)p$  neighbors and fully connect them to form a clique. Furthermore we introduce *local* dynamics on the lattice by applying the following local rules to a randomly chosen site: (i) if the site is empty: introduce a particle, (ii) if the site is occupied: move the particle to a randomly chosen neighboring site. If the application of a rule conflicts with the hard-core constraint, the rule is not applied. The time 1 MCs corresponds again to choosing  $N$  times a site at random. Fig. 10 shows the particle density that the initially empty system ( $t = 0$  MCs) has reached at MC-time  $t = 100\,000$  MCs. The error can be estimated to less than 0.1 % by comparing the results for different realizations of the graph. The asymptotic behavior of the density as a function of time can be characterized by the following observations. The density at  $t = 50\,000$  MCs ( $t = 75\,000$  MCs) is about 99.96 % (99.99 %) of the density at  $t = 100\,000$  MCs for small  $p$  and about 99.86 % (99.95 %) for great  $p$ . These figures illustrate that the compaction process becomes very slow in the second half of the simulated time frame. We do not expect the system to equilibrate on a finite time scale due the presence of glassy states. The quality of the numerical results, which constitute lower bounds for the exact values of  $\rho_\infty$ , is thus determined by the finiteness of the simulated systems and the simulated times which were chosen maximal within the limits of reasonable computation time.

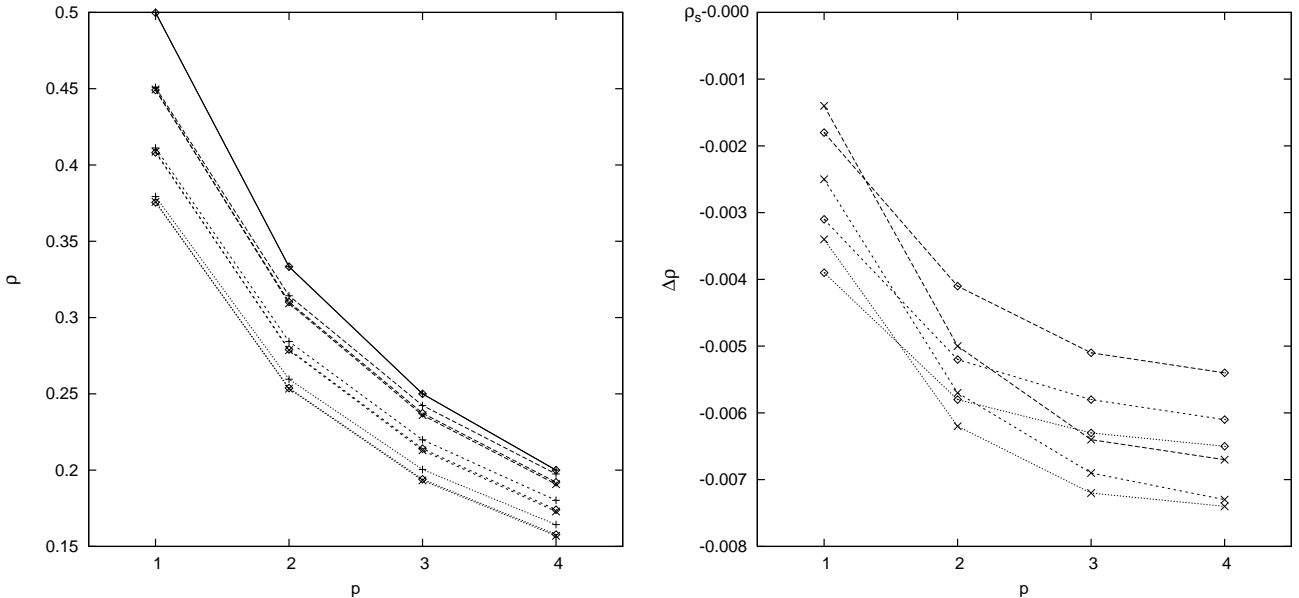


FIG. 10: Left: particle density  $\rho_\infty$  of a close-packing (+) and density  $\rho_d$  with maximal complexity (x) from the 1RSB solution compared with numerical lower bounds ( $\diamond$ ) for  $\rho_\infty$  (from top to bottom:  $k = 1, 2, 3, 4$ ). For  $k = 1$ ,  $\rho_\infty$  and  $\rho_d$  coincide. Right: the difference of  $\rho_d$  (x) and the numerical bound ( $\diamond$ ) to  $\rho_\infty \equiv \rho_s$  is shown for  $k = 2, 3, 4$  (top to bottom).

We notice that the 1RSB results for  $\rho_\infty$  are never violated by the numerical bounds. In the case  $k = 1$  the agreement between numerical and analytic results is very good which can be understood *e.g.* assuming  $p = 1$  where the “random” graph forms simply a circle which can be always packed in the crystalline ground state up to a misfit if  $N$  is odd. For  $k > 1$  the numerical bound stays always below  $\rho_\infty$  with a gap that grows with increasing  $p$  up to 4.0 %. On the other hand, we find a good agreement of the numerical bounds with the results for  $\rho_d$ . We shall explain this observation with a remark on the configuration space structure as obtained within the 1RSB solution.

We have assumed as a starting point for the derivation of the 1RSB cavity equation that a non-vanishing complexity is equivalent to the presence of an exponential (in  $N$ ) number of metastable states in the configuration space (*ergodicity breaking*). As different metastable states are only connected via configurations of lower densities any local algorithm, trying to increase the number of particles in every step, gets trapped in a metastable state. Using the definition of the complexity (20) it becomes clear that the state in question will have almost always a particle density  $\rho \simeq \rho_d < \rho_\infty$  which maximizes the complexity (cf. Fig. 9). The numerical bounds that result from a local algorithm give indeed strong indication that the concepts of the 1RSB formalism have a very concrete meaning for algorithmically induced as well as physical dynamics.

Note that there is recent work by Montanari and Ricci-Tersenghi who performed numerical cooling experiments for  $p$ -spin glasses [16], a model which is somewhat similar to our lattice gas model. The behavior for different cooling-rates underlines the relevance of the so called iso-complexity curves. In this context, the numerical experiments performed in our study constitute a limiting case of very high compaction-rate which would lead to densities significantly below  $\rho_\infty$  if the particle movement, which has no equivalent in the spin-glass context, was omitted. An investigation for different compaction-rates might give interesting complementary insights concerning the glassy phase of the lattice gas.

We conclude with the remark that there is *a priori* no indication for the correctness of the results that were calculated under the restrictions of the 1RSB ansatz. In the next section we shall sketch the baselines of a stability theory for 1RSB in order to check the reliability of the preceding results.

## B. Stability analysis of the 1RSB solution

In this section we give a brief summary of concepts concerning the local stability analysis of a 1RSB solution towards a 2RSB solution. A detailed discussion of the topic was given by Rivoire *et al.* [9] for the case a Bethe lattice gas which shares common properties with the system under study.

We start with the introduction of the 2RSB formalism. Compared to the 1RSB solution which was based on the organization of configurations in states, 2RSB acts on the level of states by assembling states in clusters to which we attribute grand-canonical potentials  $\omega_c$ . The number of states within a cluster is given by referring to  $\omega_c$ :

$$\mathcal{N}_s(\omega_s) \sim e^{Ny_s(\omega_s - \omega_c)}, \quad (66)$$

where  $y_s$  must be understood in analogy to Eq. (25) as the slope of the complexity of the states within the cluster. Using this relation as a starting point, the 1RSB cavity equation can be derived with the same arguments as in section V A yielding

$$\hat{P}[\{P^{jl}\}](x) \propto \int \prod_{j=1}^k \prod_{l=1}^p dx^{jl} P^{jl}(\{x^{jl}\}) \delta(x - \hat{x}(\{x^{jl}\})) e^{-y_s \Delta \Omega_{\text{iter}}(\{x^{jl}\})}, \quad (67)$$

when we discard the homogeneity assumption of the distributions  $P^{jl}$ . The shape of the equation invites to iterate the transfer which starts with the recursion  $\hat{x}(\{x^{jl}\})$  to deliver the 1RSB equation through the introduction of field distributions. Concretely, this means to start with the recursion  $\hat{P}[\{P^{jl}\}]$  and assume distributions of field distributions (clustering). As in the 1RSB derivation we introduce the number of clusters with grand-canonical potential  $\omega_c$  with respect to a reference point  $\omega_0$ :

$$\mathcal{N}_c(\omega_c) \sim e^{Ny_c(\omega_c - \omega_0)} \quad (68)$$

The clustering is realized by the introduction of distributions  $Q[P]$  for the field distributions. Using the arguments from section V A the so-called 2RSB cavity equations can be derived:

$$Q[P] \propto \int \prod_{j=1}^k \prod_{l=1}^p \mathcal{D}P^{jl} Q[P^{jl}] \delta(P - \hat{P}[\{P^{jl}\}]) e^{-y_c \Delta \Phi_{\text{iter}}(\{P^{jl}\})}. \quad (69)$$

where  $\Delta \Phi_{\text{iter}}$  is the change in grand-canonical potential corresponding to one step of the iteration  $\hat{P}[\{P^{jl}\}]$ . It can be obtained by evaluating  $\Delta \Omega_{\text{iter}}$  with respect to the distributions  $P^{jl}$ :

$$e^{-y_s \Delta \Phi_{\text{iter}}(\{P^{jl}\})} = \int \prod_{j=1}^k \prod_{l=1}^p dx^{jl} P^{jl}(x^{jl}) e^{-y_s \Delta \Omega_{\text{iter}}(\{x^{jl}\})}. \quad (70)$$

The hierarchical scheme of distributions can be continued to higher levels of RSB, leading to full replica symmetry breaking (*frsb*) in the limit of infinite continuation. A proof for the correctness of a 1RSB solution would require to show that every description in higher levels of RSB coincides with the 1RSB description. This is of course not feasible if only the 1RSB solution is explicitly known. In this case one can show the local stability of the 1RSB solution toward 2RSB which is believed to be a good indication for the correctness of the 1RSB solution as no example for a discontinuous transition from 1RSB to RSB of higher levels is known so far.

It was shown by Montanari and Ricci-Tersenghi that there are two possible kinds of instabilities that may occur [19]. These result from two different descriptions of a 1RSB solution within the 2RSB formalism. One way is to assume the existence of a single trivial cluster where the states are given by  $P^*(x)$ , with  $P^*$  being the 1RSB solution. Thus we have  $Q[P] = \delta[P - P^*]$  and the corresponding instability can be detected by making the ansatz  $Q[P] = f[P - P^*]$  where  $f$  is a functional with support around the null function. This corresponds to an assembling of the states that organize in clusters. The process is called *aggregation of states* and the instability is classified type I. The second possibility consists in encoding the field distribution  $P^*(x)$  in the cluster structure while the states are trivial. For discrete  $P^*$  we write  $P^* = \sum_a p_a \delta_a$  with  $\delta_a(\cdot) = \delta(\cdot - a)$ . The cluster structure is then given by  $Q[P] = \sum_a p_a \delta[P - \delta_a]$  and the instability is detected by  $Q[P] = \sum_a p_a f_a[P - \delta_a]$  with  $f_a$  having support around the null function. At the instability each state can be considered as a germ giving birth to a cluster. The process is called *fragmentation of states* and the instability is classified type II.

We shall not stress on the details of the concrete calculations which can be found in the literature for various models including combinatorial problems [9, 17, 18, 19, 20, 21, 22].

In order to investigate the stability of the 1RSB solution in the close-packing limit ( $\mu \rightarrow \infty$ ) we focus on the type-I instability. We note that there is a strong analogy between the calculation of the spin-glass instability, which was detected by putting  $P(x) = f(x - x^*)$  where  $f$  is a smeared  $\delta$ -function, and the ansatz  $Q[P] = f[P - P^*]$  suitable to find the type I instability. By transporting the calculations for the spin-glass instability to the next higher level in the RSB hierarchy the stability criterion  $kp |\lambda_{\max}(y)|^2 < 1$ , which reads precisely like Eq. (39), has been derived by Rivoire *et al.* [9]. Here  $\lambda_{\max}(y)$  is the eigenvalue of greatest modulus of the matrix

$$A(y) = \begin{pmatrix} \frac{\partial \hat{p}_0}{\partial p_0} & \frac{\partial \hat{p}_0}{\partial p_1} \\ \frac{\partial \hat{p}_1}{\partial p_0} & \frac{\partial \hat{p}_1}{\partial p_1} \end{pmatrix},$$

which is the Jacobian matrix associated with the iteration of the 1RSB field distributions Eq. (58).

A computation of  $\lambda_{\max}(y)$  yields that we have  $kp |\lambda_{\max}(y)|^2 > 1$  at  $y = y_d$  as well as  $y = y_s$  for all the cases shown in Fig. 10, *i.e.* the 1RSB solution is locally unstable toward 2RSB. We can conclude that the results for  $\rho_d$  and  $\rho_\infty$  that were derived in the 1RSB context are not exact. Following the general belief that the instability of a 1RSB solution indicates *frsb*, this would even mean  $\rho_s = \rho_d$  for  $\mu \rightarrow \infty$ , which is not suggested by the numerical findings. It must however be considered that a system cannot be brought instantaneously to infinite  $\mu$  via numerical compaction. Under the action of a MC-algorithm the simulated system will pass through a chain of genuine non-equilibrium states. By mapping these on equilibrium states according to their density we can approximately attribute a chemical potential  $\mu(t)$  to the system. It might seem more adequate to rely on a stability analysis of the 1RSB solution for  $\mu = \mu_d$  in order to decide if the compacted system is governed by metastable states. Unfortunately, this analysis seems to be out of reach for present analytical techniques.

## VII. CONCLUSION AND OUTLOOK

To conclude, we have investigated in great detail the thermodynamic behavior of a hard-sphere lattice gas model on generalized Bethe lattices.

On usual Bethe lattices, which do not contain (short) loops, the model shows a very simple behavior: At low density, the system is found in a liquid phase, and the local density is homogeneous. At a certain point, the system undergoes a second-order freezing transition. The character of this transition depends on the global graph structure: The frozen phase is either crystalline (if long loops of odd length are almost absent in the graph), or it is given by a spin-glass phase (if the Bethe lattice is defined as a regular random graph, and the crystalline structure is inconsistent with the large-scale structure of the graph).

The introduction of short loops changes this behavior drastically. We have therefore studied generalized Bethe lattices, which are locally characterized by the existence of many short loops, but on a coarse-grained level form locally tree-like hyper-graphs. This mixed structure allows for an analytical solution of the hard-sphere lattice gas.

Again, the low-density phase describes a spatially homogeneous liquid. If compactified, the system undergoes either a first-order crystallization transition or a discontinuous glass transition which is characterized by a broken replica symmetry, and by the existence of an exponentially large number of metastable states. We also find more exotic

high-density phases which are at least metastable and can thus be found also in numerical simulations. The first of these phases is an inverse-crystalline one. Its sublattice densities are inverted, as compared to the densest crystalline packing. For even higher density, this phase becomes unstable with respect to a crystalline glass transition: Even if the local densities are frozen to random values, their distributions are organized in a regular, i.e. inverse crystalline manner.

This means that hard-sphere lattice gases on generalized Bethe lattices may serve as valid, microscopically motivated and analytically tractable mean-field models for the glass transition. Do they, however, also present good approximations to the behavior in low dimensions? The hard-sphere model is in fact well studied on various two- and three-dimensional lattices, the most famous cases are the hard-hexagon model and its solution by the corner-transfer matrix [23, 24, 25], and the three-dimensional cubic lattice [26] which can be analyzed by means of series expansions. These two cases show second-order crystallization transitions. In [7] we have, however, introduced a finite-dimensional lattice mimicking the structure of the generalized Bethe lattice, and this model shows in fact a glass-like slowing down. The latter is, however, much less pronounced due to the existence of activated processes in finite dimensions.

At this point, another remark concerning the relation of the generalized Bethe-lattice models to  $p$ -spin glass models is necessary. The latter model class was extensively used in particular in the last decade in the context of the glass transition [3, 5]. On one hand, they allow for an analytical treatment of the model statics and dynamics, the latter being formally equivalent to the mode-coupling approach to more realistic glass-forming liquids.  $p$ -spin glasses are, however, completely missing a microscopic motivation. One point here is the existence of unphysical multi-spin interactions. If we look, however, to our generalized Bethe-lattice model, the introduction of cliques effectively introduces multi-site interactions – only one site per clique can be occupied – even if these are defined via groups of pair interactions. This allows to reinterpret also the  $p$ -spin interactions in spin-glass models as a kind of coarse grained effective interaction.

All the considerations in this paper are restricted to the thermodynamic, i.e. equilibrium behavior of the model. In particular in the glassy regions, we know that the dynamics becomes very slow, and the system is practically always out of equilibrium. The analytical description of the dynamics of finite-connectivity models is, however, a much more involved problem, and it is to a large extent an unsolved one. In a subsequent publication, we will confront our findings on the static behavior with an approximate analysis of the dynamics [13]. The approach taken there is related to a projective approximation scheme introduced in [27, 28] in the context of algorithms for combinatorial optimization, and then applied to simple Ising ferromagnets in [29]. Within this scheme, the dynamics is projected to the dynamics of a small set of global observables, and the resulting equations are closed on the basis of a pseudo-equilibrium ansatz in an enlarged ensemble. The selection of this generalized ensemble, and the technical realization of the projection are based on the tools developed in this article, and therefore will form a natural continuation of the present work.

**Acknowledgment:** We are grateful to A.K. Hartmann, G. Semerjian and A. Zippelius for many interesting discussions. HHG acknowledges also the hospitality of the ISI Foundation in Turin, where some of the final steps in this project were done.

---

[1] W. Götze, *Liquids, freezing, and glass transition*, Les Houches (1989).

[2] C.A. Angell, Science **267**, 1924 (1995).

[3] J.P. Bouchaud, L.F. Cugliandolo, J. Kurchan, and M. Mézard, in *Spin Glasses and Random Fields*, ed. A.P. Young (World Scientific, Singapore, 1998).

[4] F. Ritort and P. Sollich, Adv. Phys. **52**, 219 (2003).

[5] L.F. Cugliandolo, *Dynamics of glassy systems*, Lecture notes, Les Houches (2002).

[6] G. Biroli and M. Mézard, Phys. Rev. Lett. **88**, 025501 (2002).

[7] M. Weigt and A. K. Hartmann, Europhys. Lett. **62**, 533 (2003).

[8] M. Pica Ciamarra, M. Tarzia, A. de Candia and A. Coniglio, Phys. Rev. E **67**, 057105 (2003).

[9] O. Rivoire, G. Biroli, O. C. Martin and M. Mézard, Eur. Phys. J. B **37**, 55-78 (2004).

[10] M. Sellitto, G. Biroli, and C. Toninelli, to app. in Europhys. Lett. (2005).

[11] M. Mézard, G. Parisi and M. A. Virasoro, *Spin Glass Theory and Beyond*, (World Scientific, Singapore, 1987).

[12] M. Mézard and G. Parisi, Eur. Phys. J. B **20**, 217-233 (2001).

[13] H. Hansen-Goos and M. Weigt, in preparation.

[14] L. K. Runnels, J. Math. Phys. **8**, 2081 (1967).

[15] R. Monasson, Phys. Rev. Lett. **75**, 2847-2850 (1995).

[16] A. Montanari and F. Ricci-Tersenghi, Phys. Rev. B **70**, 134406 (2004).

[17] O. Dubois, R. Monasson, B. Selman and R. Zecchina (eds.), Theor. Comp. Sci. **265**, issue 1-2 (2001).

[18] M. Mézard, G. Parisi and R. Zecchina, Science **297**, 812 (2002); M. Mézard and R. Zecchina, Phys. Rev. E **66**, 056126 (2002).

[19] A. Montanari and F. Ricci-Tersenghi, Eur. Phys. J. B **33**, 339 (2003).

- [20] A. Montanari, G. Parisi and F. Ricci-Tersenghi, J. Phys. A: Math. Gen. **37**, 2073-2091 (2004).
- [21] S. Mertens, M. Mézard and R. Zecchina, preprint [cs/0309020](https://arxiv.org/abs/cs/0309020) (2003).
- [22] F. Krzakala, A. Pagnani and M. Weigt, Phys. Rev. E **70**, 046705 (2004).
- [23] R.J. Baxter, J. Phys. A **13**, L61 (1980).
- [24] R.J. Baxter, *Exactly Solved Models in Statistical Mechanics*, (Academic Press, London 1982).
- [25] R.J. Baxter, Ann. Comb. **3**, 191 (1999).
- [26] D.S. Gaunt, J. Chem. Phys. **46**, 3237 (1967).
- [27] G. Semerjian and R. Monasson, Phys. Rev. E **67**, 066103 (2003).
- [28] W. Barthel, A.K. Hartmann, and M. Weigt, Phys. Rev. E **67**, 066104 (2003).
- [29] G. Semerjian and M. Weigt, J. Phys. A **37**, 5525 (2004).